Dynamics Governing a Simulated Bow-and-Arrow-Type Mesoscale Convective System

Shushi Zhang, ^{a,b} David B. Parsons, ^c Xin Xu[®], ^{d,e} Jisong Sun, ^b Tianjie Wu, ^a Abuduwaili Abulikemu, ^f Fen Xu, a Gang Chen, a Wenqiang Shen, Elhang Liu, Xidi Zhang, i.d Kun Zhang, and Wei Zhang Kun Zhang, i.d Kun Z

^a Key Laboratory of Transportation Meteorology of China Meteorological Administration, Nanjing Joint Institute for Atmospheric Sciences, Nanjing, China ^b State Key Laboratory of Severe Weather, Chinese Academy of Meteorological Sciences, Beijing, China ^c School of Meteorology, University of Oklahoma, Norman, Oklahoma ^d Key Laboratory of Mesoscale Severe Weather (Ministry of Education), School of Atmospheric Sciences, Nanjing University, Nanjing, China ^e China Meteorological Administration Radar Meteorology Key Laboratory, Nanjing, China f Key Laboratory of Oasis Ecology (Ministry of Education), College of Resources and Environment Sciences, Xinjiang University, Urumqi, China g Zhejiang Provincial Meteorological Observatory, Hangzhou, China ^h Wuxi First Research Institute, Wuxi, China ⁱ National Meteorological Center, China Meteorological Administration, Beijing, China ¹ Huaihua Meteorological Bureau, Huaihua, China ^k Pingliang Meteorological Bureau, Pingliang, China

(Manuscript received 31 March 2022, in final form 20 October 2022)

ABSTRACT: The bow-and-arrow Mesoscale Convective System (MCS) has a unique structure with two convective lines resembling the shape of an archer's bow and arrow. These MCSs and their arrow convection (located behind the MCS leading line) can produce hazardous winds and flooding extending over hundreds of kilometers, which are often poorly predicted in operational forecasts. This study examines the dynamics of a bow-and-arrow MCS observed over the Yangtze-Huai Plains of China, with a focus on the arrow convection provided. The analysis utilized backward trajectories and Lagrangian vertical momentum budgets to simulations employing the WRF-ARW and CM1 models. Cells within the arrow in the WRF-ARW simulations of the MCS were elevated, initially forming as convectively unstable air within the low-level jet (LLJ), which gently ascended over the cold pool and converged with the MCS's mesoscale convective vortex (MCV) at higher altitudes. The subsequent ascent in these cells was enhanced by dynamic pressure forcing due to the updraft being within a layer where the vertical shear changed with height due to the superposition of the LLJ and the MCV. These dynamic forcings initially played a larger role in the ascent than the parcel's buoyancy. These findings were bolstered by idealized simulations employing the CM1 model. These results illustrate a challenge for accurately forecasting bow-andarrow MCSs as the updraft magnitude depends on dynamical forcing associated with the interaction between vertical shear associated with the environment and due to convectively generated circulations.

KEYWORDS: Convective storms/systems; Dynamics; Mesoscale processes

1. Introduction

Convection is often organized into mesoscale convective systems (MCSs) containing both convective cells and large areas of stratiform rainfall that produce precipitation extending over areas in excess of $\sim 10000 \text{ km}^2$ (Houze 2004). The ability to accurately simulate MCSs in global numerical weather prediction (NWP) systems (e.g., Bechtold et al. 2014), convection-allowing models (CAMs; e.g., Haiden et al. 2018) and climate models is a critical societal need (e.g., Tseng et al. 2018). For example, it is well established that rainfall from convective systems is often beneficial, but can also be associated with significant detrimental impacts worldwide, such as flash floods, hail, high winds and so on.

One type of MCS is the "bow and arrow" MCS, which was first documented by Keene and Schumacher (2013). This term refers to the bow-shaped pattern of radar echoes at the leading edge of the system and a second convective line behind

arrow in the radar imagery (Fig. 1). In this type of MCS, the bow-shaped leading convective line is often associated with severe, damaging winds at the surface (e.g., Johns 1993; Przybylinski 1995; Davis et al. 2004). A recent investigation by Mauri and Gallus (2021) noted multiple challenges of accurately forecasting bow-shaped echoes and explored the dependence of the generation of severe weather associated with these bow systems on environmental conditions. For bowand-arrow MCSs, an additional arrow region of convection develops at some distance behind and nearly perpendicular to the leading convective line (e.g., Keene and Schumacher 2013; Hitchcock and Schumacher 2020; Parker 2021). The convection within the arrow is also sometimes referred to as rearward off-boundary development (ROD; Peters and Schumacher 2014).

the leading edge of the system that resembles an archer's

The bow-and-arrow MCS is also considered a type of "back building" MCS that can produce locally heavy rainfall and flooding. In the case of a bow-and-arrow MCS, surface rainfall results from the combination of the leading line of intense convection within the bow, stratiform rain behind the bow,

Corresponding author: Xin Xu, xinxu@nju.edu.cn

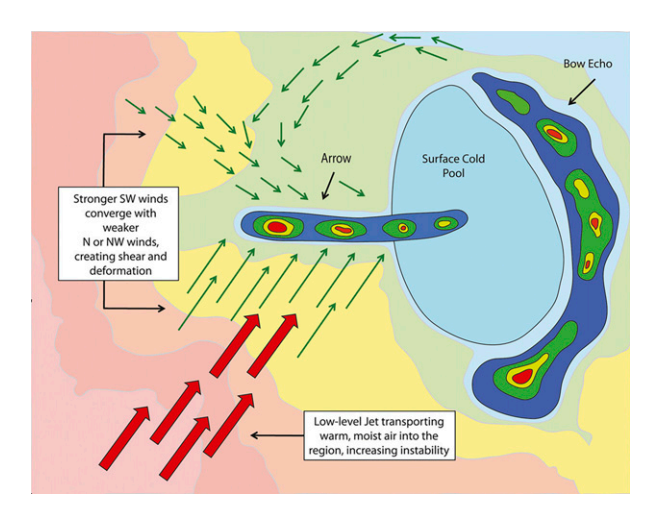


FIG. 1. Schematic diagram showing the important components of the bow-and-arrow MCS with the thick red arrows representing the low-level jet, the thin green arrows representing wind direction and speed for all pressure levels, and the colored contours representing isotherms. From Keene and Schumacher (2013).

and then additional heavy rainfall from strong convective cells within the arrow repeatedly redeveloping (i.e., back building) behind the leading line of convection. If the series of convective cells within the arrow pass over the same region for an extended period of time (i.e., training echoes), heavy rainfall and flooding will often occur. Studies have found that back-building MCSs are not only associated with flash flooding but also with potentially damaging severe winds and hail (e.g., Chappell 1986; Schumacher and Johnson 2005; Keene and Schumacher 2013; Hitchcock and Schumacher 2020). As noted by Hitchcock and Schumacher (2020), even in an initially horizontally homogeneous environment, different portions of a bow-and-arrow MCS can have different propagation mechanisms and different inflow layers supporting deep convection. Thus, it is not surprising that predicting the development of MCSs has long been a challenge for forecasters (e.g., Olson et al. 1995; Corfidi et al. 1996; Snively and Gallus 2014; Lawson and Gallus 2016) and that it is difficult to accurately simulate these bowand-arrow events in numerical models (Keene and Schumacher 2013).

Efforts to better understand the initiation and maintenance of back-building MCSs can be traced back to Miller (1978), who found such MCSs occurred along outflows produced from previous convection. Corfidi et al. (1996) and Corfidi (2003) also investigated back-building MCSs and found that their propagation direction is generally dictated by the location of the maximum low-level convergence along the cold pool within a conditionally unstable environment. In contrast, based on their analysis of six back-building cases, Schumacher and Johnson (2009) found no apparent surface boundaries nearby, but noted the presence of a midlevel cyclonic vorticity maximum generated by the MCS that is often referred to as a mesoscale convective vortex (MCV). The interaction of this cyclonic circulation with the low-level jet (LLJ) led to lifting,

destabilization, and convective initiation (CI) just south of the vortex center.

Subsequently, Keene and Schumacher (2013) investigated 14 bow-and-arrow type of back-building MCSs and found that the arrow convection formed behind or sometimes above the cold pool behind the bow (Fig. 1). Specifically, the arrow echoes were located near where southwesterly flow associated with the LLJ juxtaposed with northwesterly flow to the rear of the MCS. In the archetypal case described by Keene and Schumacher (2013), the cold pool played an important role in supporting the ascent in an environment complicated by the presence of a preexisting baroclinic zone. Their study concluded that warm-air advection and gradual isentropic lifting contributed to adequate convergence to support CI associated with the convection within the arrow. Keene and Schumacher (2013) also hypothesized that the arrow's linear orientation may have been due to a combination of increased wind speeds and horizontal shear within this region. Peters and Schumacher (2016) also proposed that the linearity and orientation of the arrow convection were influenced by the deformation and vertical wind shear along the orientation of the arrow.

Studies have also suggested that other mechanisms may be playing a major role in supporting the formation of the convective arrow. For example, Schumacher and Johnson (2009) suggested that a nearly stationary low-level gravity wave, rather than a cold pool, could be responsible for the ascent. This hypothesis was subsequently substantiated by idealized numerical simulations (Schumacher 2009). More recently, Hitchcock and Schumacher (2020) found that the nocturnal stable boundary layer (NSBL) likely influenced the MCS structure by impacting the ability of convective storm's downdrafts to reach the surface. Thus, an elevated intrusion layer was generated in simulations undertaken in the Hitchcock and Schumacher (2020) study rather than a surface-based cold pool as in Keene and Schumacher (2013).

While these previous studies illustrate the potential role of various mesoscale processes (e.g., deformation, vertical wind shear, gravity waves, the MCV, preexisting baroclinicity and elevated and surface-based cold pools) to influence arrow convective development, to date there has not been a detailed nonhydrostatic dynamical analysis of the processes driving the vertical motions within the arrows. Our study aims to undertake a detailed dynamical analysis to quantify the relative importance of the different processes driving vertical motions within the convective cells defining the arrows, including buoyancy and the various dynamical processes that contribute to vertical pressure perturbations (i.e., fluid extension, horizontal and vertical shear, horizontal curvature, vertical twisting). We will then seek to place these dynamical findings within the context of both the environmental properties and the circulations generated by the bow-and-arrow MCS. Our study supports the hypothesis that dynamical processes, such as the updraft interacting with the vertical shear associated with the superposition of the LLJ and the MCV, significantly contribute to the magnitude of the updrafts and organization of convective cells within the arrow.

The bow-and-arrow MCS studied herein was observed over the Yangtze–Huai Plains of China in the presence of a strong

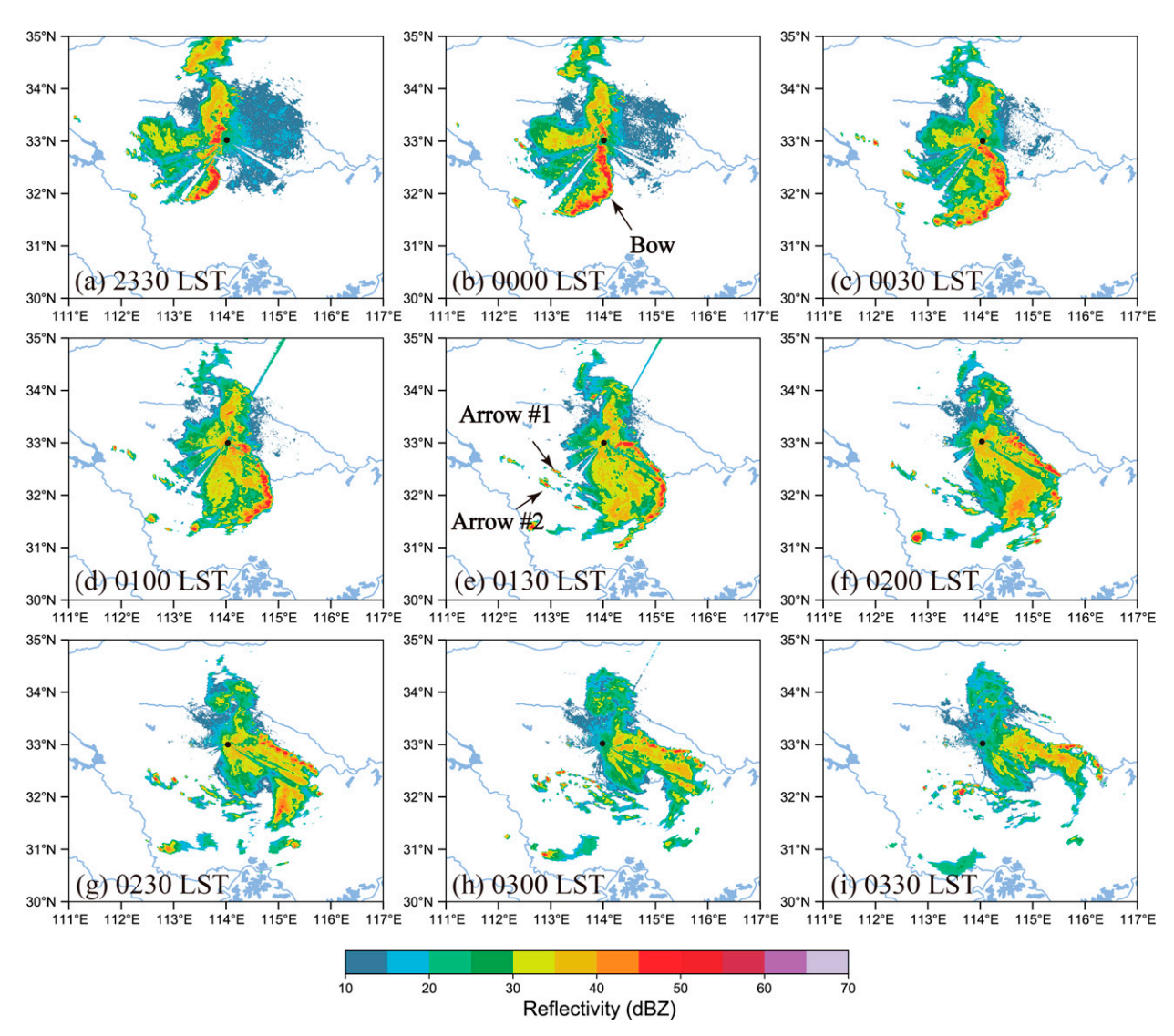


Fig. 2. (a)–(i) Radar reflectivity (dBZ) from the ZMD radar at an elevation angle of 0.47° from 2330 LST 5 to 0330 LST 6 Jun 2016. The black arrows in (e) indicate the location of the two convective lines (arrows) behind the leading convective line (bow) [indicated by the black arrow in (b)], and the black circles indicate the location of the ZMD radar.

NSBL. This MCS was previously investigated by Zhang et al. (2020), which found that the MCS was characterized by a bore that evolved from a type-C to a type-B bore structure ahead of the "bowing" leading line of convection, a common phenomenon of bores over China (Zhang et al. 2022). This current study utilizes numerical simulations and dynamical analyses to specifically focus on the mechanisms initiating and maintaining two trailing arrows of convection behind the leading convective line.

The remainder of this paper is organized as follows. A brief summary of the observational analysis presented in Zhang et al. (2020) is discussed in section 2 focusing on the arrow portions of this MCS. The method is presented in section 3. An overview of the MCS structure and evolution of the WRF simulation are presented in section 4 followed by a detailed

investigation of the dynamic forcing mechanisms and physical explanations of the interactions between the LLJ and MCV in section 5. Section 6 discusses the results from the CM1 model with the findings summarized, and the implications are presented in section 7.

2. Case overview

As described in Zhang et al. (2020), the MCS investigated in this study was first observed over the elevated terrain west of the Yangtze–Huai Plains on 5 June 2016 and subsequently evolved during the night into the early morning hours of 6 June 2016 (Fig. 2). The synoptic environment included a low pressure center at 850 hPa, along with a broad upper-level trough and an embedded weak shortwave trough at 500 hPa.

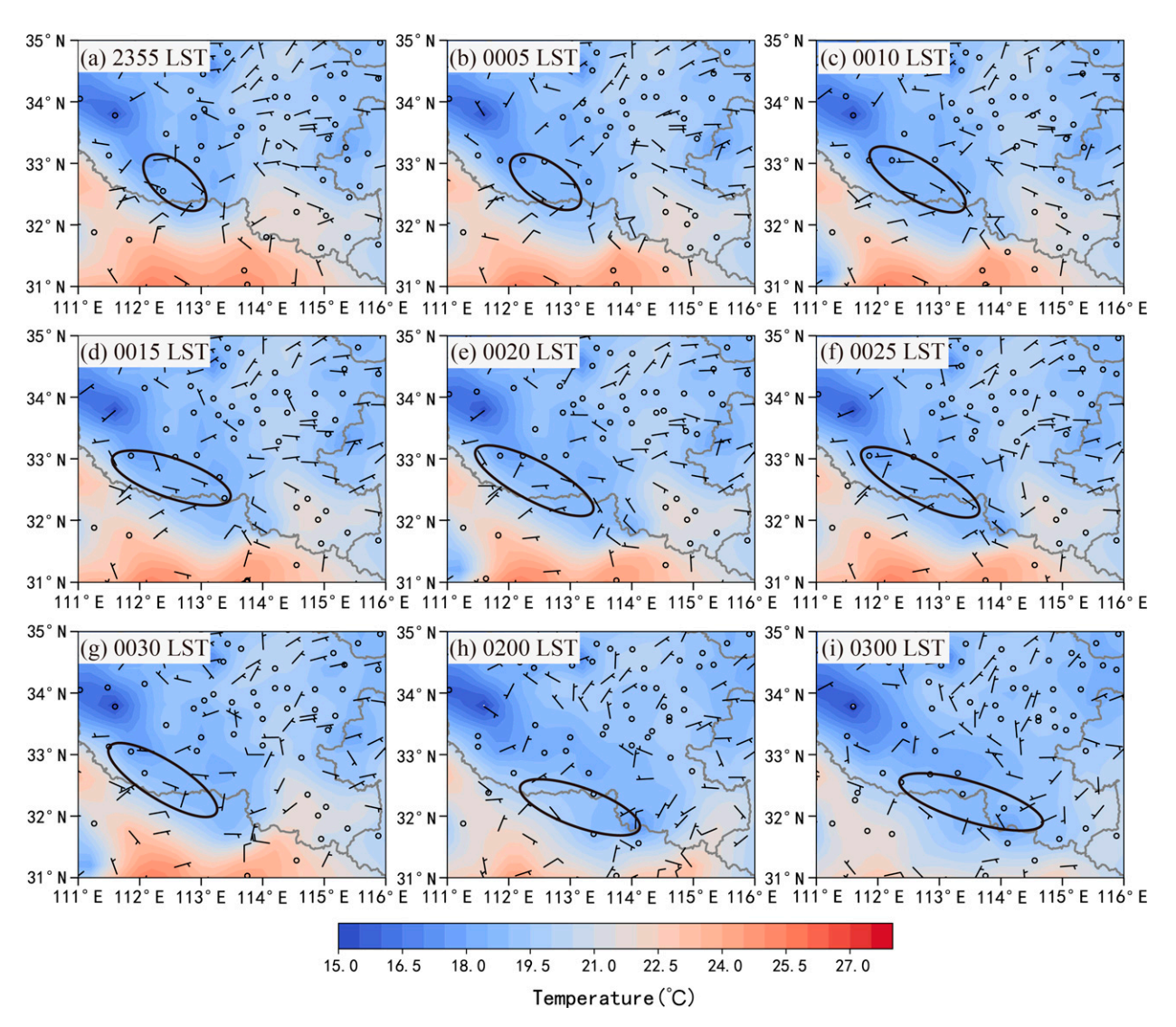


Fig. 3. The 2D linearly interpolated surface temperature observations (shading; $^{\circ}$ C), observed total surface winds [wind barbs; kt (1 kt \approx 0.5 m s⁻¹)] from 2355 LST 5 to 0300 LST 6 Jun 2016 as follows: (a) 2355, (b) 0005, (c) 0010, (d) 0015T, (e) 0020, (f) 0025, (g) 0030, (h) 0200, and (i) 0300 LST. Black-outlined ellipses indicate the location of the arrow convective bands and convective cluster originating from the earlier arrow convective bands behind the MCS leading line.

Initially, conditions were relatively unfavorable for deep convection, with little CAPE, large CIN and a strong low-level inversion (Figs. 2 and 3 in Zhang et al. 2020). However, as discussed in Zhang et al. (2020), a LLJ brought more favorable conditions (e.g., CAPE and vertical shear) for deep convection later in the night.

Observations from the Zhumadian (ZMD) radar (Fig. 2) depict the structure and evolution of the convective arrows. The arrows appeared as lines of convective cells with a lifetime of ~2.5 h and a maximum length of ~170 km. Convective cells were initially evident behind the bow at 0030 LST (Fig. 2c), subsequently organizing into a linear structure by 0100–0200 LST (Figs. 2d–f). From 0230 to 0300 LST (Figs. 2g–i), the convective cells in the wake of the MCS's leading edge then evolved into a larger area of convection

extending to cover a region of $\sim 13\,500~\text{km}^2$ behind the remnants of the bow echo.

Surface analysis (Fig. 3) showed that this MCS formed in a baroclinic environment as a warm air mass was present south of the MCS, with a cold pool noted behind the leading edge of the MCS. Keene and Schumacher (2013) also noted the presence of baroclinicity in bow echo environments over North America. However, a -3°C surface temperature perturbation was associated with the cold pool in Fig. 3, which is weaker than cold pools often associated with MCSs over the Great Plains. This difference could be due to a generally moister convective environment over China (Liu and Moncrieff 2017), although an alternate explanation for the weaker cold pools in this case could be the impacts of earlier convection on the environment ahead of the MCS.

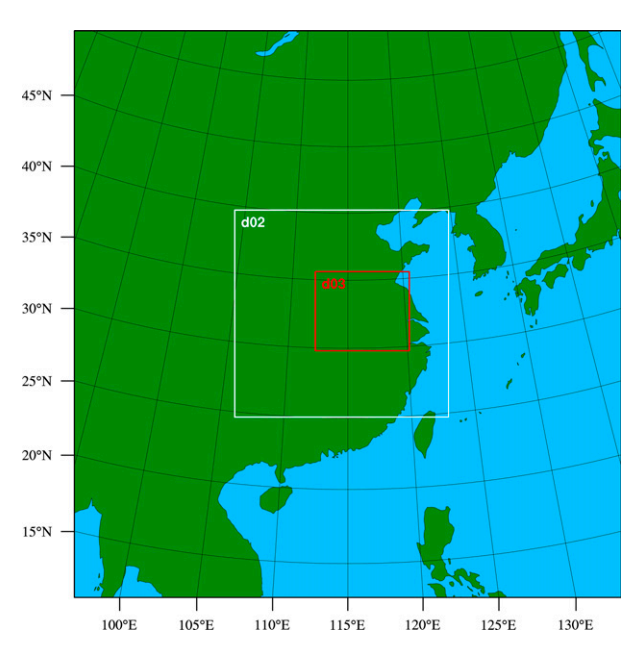


FIG. 4. Domain configurations used in the WRF Preprocessing System and in the simulations. The figure encompasses the outer domain with a horizontal grid spacing of 9 km. The two inner domains at 3- and 1-km resolution are indicated by the boxes labeled d02 and d03, respectively.

The convective cells composing the arrows in this MCS formed far from the cold pool boundary in Fig. 3 consistent with ROD discussed in Peters and Schumacher (2014), and with the generation of an extensive cold pool as the MCS matured (Fig. 3i). The development of the convective arrows far from the leading edge of the cold pool suggests that gradual quasi-isentropic, rearward ascent of buoyant air over the cold pool may have played a role in the initial formation of the arrows as in Schumacher (2009). However, the available observations alone are insufficient to support this conclusion. Thus, we conducted real and idealized numerical simulations of this bow-and-arrow MCS and subsequently applied dynamic

analyses to understand the mechanisms driving the convective updrafts within the arrows.

3. Method

a. Design of the numerical simulations of the MCS

The design of our simulations follows that of Zhang et al. (2020), with the utilization of the WRF-ARW (version 4.0) Model (Skamarock et al. 2008) employing three two-way nested domains with horizontal resolution of 9, 3, and 1 km, respectively (Fig. 4). The initial and boundary conditions were derived from the 6-hourly, $0.703^{\circ} \times 0.702^{\circ}$ ERA Interim analysis. The simulation was conducted for 16 h beginning at 0800 LST 5 June 2016. The model grid included 49 levels in the vertical with spacing ranging from ~60 m near the surface to \sim 300 m near the model top at \sim 17 km. The details of the configuration of the WRF-ARW simulations in this study are listed in Table 1. One difference between the simulations in this study and Zhang et al. (2020) is that the model fields were output at an interval of 1 min for the innermost domain to provide sufficient time resolution for our detailed trajectory analysis.

b. Design of the idealized numerical simulations

Our idealized simulations employed Cloud Model 1 (CM1; Bryan and Fritsch 2002) as utilized in the prior studies by Schumacher (2009) and Hitchcock and Schumacher (2020). The model version (19.1) and configuration generally followed that of Hitchcock and Schumacher (2020), but with differences in the domain size and the model grid spacing. Given our focus on a dynamic analysis that included trajectories at 1-min intervals, we utilized a vertical resolution of 50 m and a horizontal resolution of 1 km with a $1000 \times 1000 \times$

The convection in our CM1 experiment was initiated by an isolated thermal with a radius of 80 km in the horizontal plane, a radius of 2 km in the vertical direction, and a +5-K potential temperature perturbation. The CM1 experiment was initialized using the sounding obtained from the WRF

TABLE 1. Summary of the ARW configuration for this study.

Attribute	Domain 1	Domain 2	Domain 3	References
Grid spacing	9 km	3 km	1 km	
Horizontal dimensions	$4581 \text{ km} \times 4419 \text{ km}$	$1674 \text{ km} \times 1728 \text{ km}$	$639 \text{ km} \times 759 \text{ km}$	
Vertical sigma levels	49	49	49	
Model top pressure	50 hPa	50 hPa	50 hPa	
ICs and LBCs	EC-interm	EC-interm	EC-interm	
Microphysics	Morrison 2-moment	Morrison 2-moment	Morrison 2-moment	Morrison et al. (2005)
Longwave radiation	CAM	CAM	CAM	Collins et al. (2004)
Shortwave radiation	CAM	CAM	CAM	Collins et al. (2004)
Surface layer	Pleim-Xiu	Pleim-Xiu	Pleim-Xiu	Pleim (2006)
Land surface model	Pleim-Xiu	Pleim-Xiu	Pleim-Xiu	Pleim (2006)
Boundary layer physics	Asymmetrical Convective Model, version 2	Asymmetrical Convective Model, version 2	Asymmetrical Convective Model, version 2	Pleim (2007)
Cumulus parameterization	Kain-Fritsch	None	None	Kain (2004)

simulation output at 0300 LST from a location upstream of the convective arrows where the southwesterly LLJ interacted with northwesterly flow from MCV aloft. This sounding contained a stable boundary layer and high CAPE aloft, recreating the condition of where the LLJ and MCV interacted in WRF model simulations.

c. Vertical momentum budgets

The dynamics of the convective cells within the arrow behind the bow echo were investigated by applying vertical momentum budgets to determine the key factors governing the dynamics of the convective updrafts. The vertical momentum budgets we utilized were proposed by Jeevanjee and Romps (2015) and applied in numerous subsequent studies (e.g., Schenkman et al. 2016; Peters 2016; Lombardo and Kading 2018; Abulikemu et al. 2019, 2020).

In this approach, the vertical acceleration is split into the buoyant (a_b) and dynamic (a_d) contributions, respectively:

$$\frac{dw}{dt} = a_b + a_d,\tag{1}$$

where a_b and a_d are separately obtained from the following Poisson equations:

$$\nabla^2(\overline{\rho}a_h) = -g\nabla_h^2\rho \quad \text{and} \tag{2}$$

$$\nabla^{2}(\overline{\rho}a_{d}) = \frac{\partial}{\partial z} \nabla \cdot [\overline{\rho}(\mathbf{V} \cdot \nabla)\mathbf{V}]. \tag{3}$$

In these equations, ρ is the total air density; g is the gravitational acceleration; ∇^2 and ∇^2_h are the three-dimensional and horizontal Laplacian operators, respectively; and \mathbf{V} is the three-dimensional wind. The term

$$a_b \left(-\frac{1}{\rho} \frac{\partial p_b'}{\partial z} - g \frac{p'}{\rho} \right)$$

is due to buoyancy effects, where p_b' is the buoyancy pressure perturbation due to spatial variations in the buoyancy field itself as discussed in Dawson et al. (2016). The term a_b is defined as the vertical acceleration owing to horizontal density variations, including both the response of the environment to the vertical acceleration and the Archimedean buoyancy $(B = g\rho'/\bar{\rho})$, where $\bar{\rho}$ is the base-state air density upstream of the arrows, and ρ' is the perturbation in density from the base state $\bar{\rho}$). Using this method, one can avoid ambiguities in the definition of the base state density, as noted in previous studies (e.g., Krueger et al. 1995; Xu and Randall 2001; Davies-Jones 2003; Torri et al. 2015; Xu et al. 2015; Abulikemu et al. 2019, 2020). The term

$$a_d \left(-\frac{1}{\rho} \frac{\partial p_d'}{\partial z} \right)$$

is the contribution to the acceleration from the vertical accelerations resulting from vertical gradients in p'_d , which is the dynamic pressure perturbation solely due to spatial variations in velocity.

As in Klemp and Rotunno (1983), the right-hand-side of Eq. (3) can be decomposed into the following five terms under the assumption of anelastic approximation, namely,

$$\nabla \cdot \left[\overline{\rho}(\mathbf{V} \cdot \nabla)\mathbf{V}\right] = \overline{\rho}_{(z)} \left[\left(\frac{\partial u}{\partial x} \right)^2 + \left(\frac{\partial v}{\partial y} \right)^2 \right], \tag{4a}$$

$$+ \overline{\rho}_{(z)} \left[\left(\frac{\partial w}{\partial z} \right)^2 \right], \tag{4b}$$

$$+ 2\overline{\rho}_{(z)} \left(\frac{\partial v}{\partial x} \frac{\partial u}{\partial y} \right), \tag{4c}$$

$$+2\overline{\rho}_{(z)}\left(\frac{\partial w}{\partial x}\frac{\partial u}{\partial z}+\frac{\partial w}{\partial y}\frac{\partial v}{\partial z}\right), \text{ and } (4d)$$

$$-\overline{\rho}_{(z)} \left\{ w^2 \frac{d^2 \ln[\overline{\rho}_{(z)}]}{dz^2} \right\}. \tag{4e}$$

The terms (4a) and (4b) denote the horizontal and vertical fluid extensions, respectively, associated with the horizontal and vertical convergence, and terms (4c) and (4d) are related to horizontal curvature and vertical twisting, respectively, associated with the horizontal and vertical wind shear. The term (4e) represents the combination of vertical velocity and the variation of density with height. The partial derivation of these terms with respect to z would appear on the right side of Eq. (3), and thus solved to determine their contributions on a_d .

As suggested by Schenkman et al. (2016) and Dawson et al. (2016), a_b and a_d were numerically solved by using the fast multigrid solver in MUDPACK (Adams 1989) through substitution into the right-hand side of Eq. (3). The Direchlet boundary conditions of $a_b = 0$ and $a_d = 0$ were specified on both the bottom and top boundaries, which Jeevanjee and Romps (2015) proposed to be the most unambiguous and optimal boundary conditions. The subdomain for this budgets analysis covers the entire area containing the arrows with 385, 385, and 193 grid points in the x, y, and z directions, respectively.

4. Overview of the WRF-simulated MCS structure and evolution

a. Horizontal pattern

The composite reflectivity of the WRF-ARW simulated bow-and-arrow MCS is shown in Fig. 5, along with the meso-scale horizontal winds and the perturbation geopotential heights at the 850-hPa level. Aspects of the MCS were relatively well reproduced in terms of the general structure and evolution (see Figs. 2 and 5), which included a bow echo that developed a comma head with rotating cyclonic flow on the northern portion of the bow and the formation of two convective arrows. Some differences also exist between the observed and simulated MCS. The location of the simulated MCS was spatially displaced to the northeast of its observational

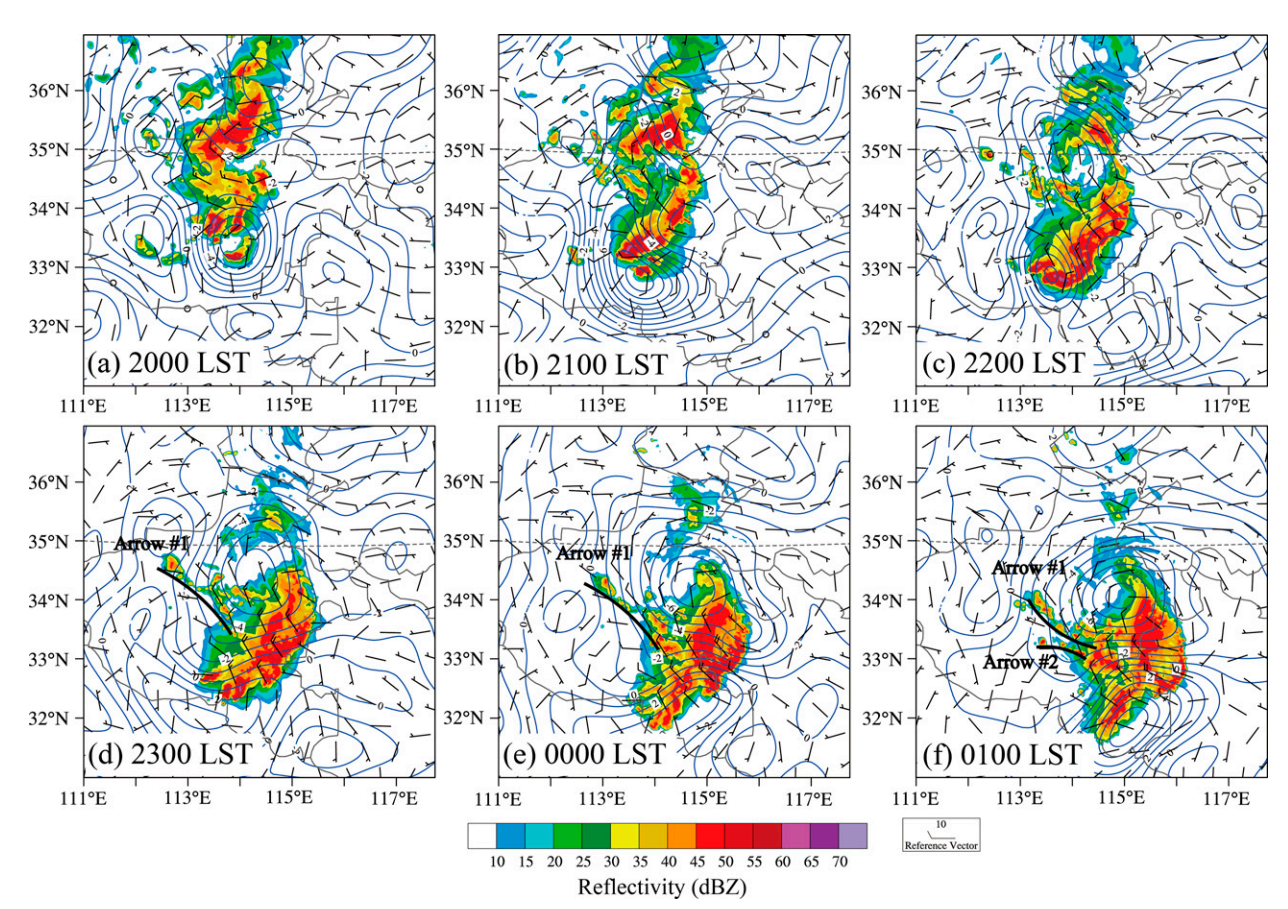


FIG. 5. Reflectivity (shading; dBZ) of domain 2, overlaid with the mesoscale height perturbations (blue contours at 1-m intervals) and the total wind (wind barbs; kt) at 850 hPa from 2000 LST 5 to 0100 LST 6 Jun as follows: (a) 2000, (b) 2100, (c) 2200, (d) 2300, (e) 0000, and (f) 0100 LST. The wind and height fields were extracted using a Barnes filter (Barnes 1973; Wei et al. 2023) to allow a direct perspective on how the associated MCV evolved. The arrows containing the convective cells are indicated by black lines.

counterpart, a common phenomenon that occurs in simulations (e.g., Squitieri and Gallus 2016; Peters et al. 2017; Vertz et al. 2021). The simulation also had stronger and more extensive convection on the southern flank of the MCS (>40 dBZ), which is a known problem that can result from short comings in the microphysical parameterization (Morrison and Milbrandt 2015).

The mesoscale wind field and geopotential height at 850 hPa (Fig. 5) provide a general view into the relationship between the MCV evolution and the formation of the convective arrows. As the MCS evolved, a cyclonic circulation with a low pressure center began to form after 2100 LST (Fig. 5b) and was clearly evident on the northern flank of the MCS at 2200 LST as an MCV (Fig. 5c). The MCV subsequently intensified (Figs. 5c–e) and dominated the MCS wind field at 850 hPa. Later in the MCS life cycle, from 2300 to 0100 LST, the arrows developed behind the MCS leading line, where LLJ-driven southwesterly flow transitioned to northwesterly flow from the MCV (Figs. 5d,f).

We now shift our attention to the evolution of the arrows. Scattered cells initially formed at 2000 LST and subsequently dissipated behind the MCS (Fig. 5a). The convection then

slowly took on a more linear orientation over the next several hours (Figs. 5b,c). At ~2300 LST, the convection behind the MCS took on a clear linear orientation representing an arrow (designated arrow 1 in Fig. 5d). A second smaller arrow (designated arrow 2) subsequently developed around 0100 LST (Fig. 5f). Both arrows formed in the convergence at the LLJ/MCV interface, suggesting the presence of a lifting mechanism responsible for CI of the cells within the arrows. This mechanism is consistent with previous findings (e.g., Schumacher and Johnson 2009).

The larger-scale environmental conditions at the 850- and 700-hPa levels are shown for 2300 and 0100 LST, respectively, when arrow 1 and 2 first formed (Fig. 6). At 850 hPa, a notable cyclonic circulation was present in the trailing region behind the MCS at both times with the circulation covering a larger horizontal extent at 0100 LST (Figs. 6a,b). The MCS was embedded within southwesterly flow at 850 hPa with the largest most unstable CAPE (MUCAPE) being transported into the region containing the arrows behind the MCS, providing an unstable environment for convection in the wake of the bow echo (Figs. 6a,b). The presence of the largest MUCAPE behind the MCS is relatively unusual, as for

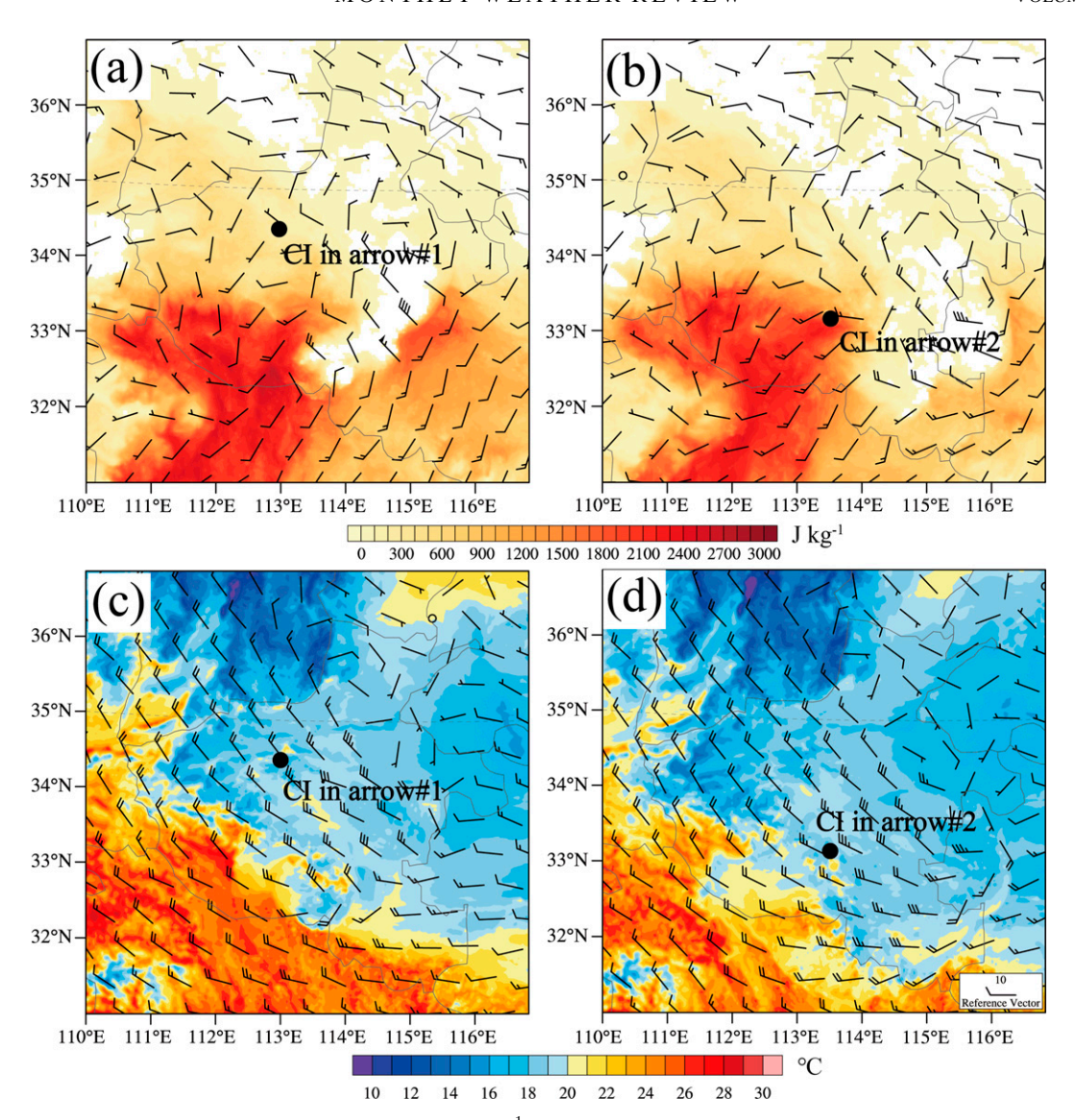


FIG. 6. (a),(b) Simulated MUCAPE (shading; J kg⁻¹) and 850-hPa total wind field (wind barbs; kt), along with (c),(d) simulated surface temperature (shading; °C) and 700-hPa total wind field (wind barbs; kt), at (left) 2300 and (right) 0100 LST. The black dots indicate the rough location of the representative convective cells in the arrows.

example, squall lines are generally maintained by lifting of unstable air at the leading edge of the MCS. The flow where the CI took place was convergent at 850 hPa, especially for arrow 2.

At 700 hPa, NW flow was present at both 2300 and 0100 LST (Figs. 6c,d). This vertical superposition of the southwesterly flow associated with the LLJ at 850 hPa and the NW flow at 700 hPa creates a layer with strong vertical shear. The surface temperature pattern (Figs. 6c,d) reveals a NW–SE-oriented baroclinic zone with warm air in the SW portion of the domain. The arrow convection is located well behind the leading edge of the cold pool so that ascent at the leading edge of the cold pool is not directly driving the formation of the arrows. However, the locations of the cells well behind the leading edge of the cold pool suggests that gradual

ascent over the cold pool likely plays a significant role in bringing parcels to their level of free convection (LFC). The MCS is located on the cold side of thermal gradient and a frontogenesis analysis (not shown) confirms that frontogenetically forced ascent is not responsible for the development of the arrows. However, the baroclinic environment may play a role in generating the MCS as bow echoes over the United States frequently form near frontal zones (e.g., Johns 1993).

b. Trajectories

Two cells from each arrow were selected to provide insight into the dynamic forcing initially driving the updrafts within the arrows (Fig. 7). For arrow 1, two of the earliest initiated cells were selected for the trajectory analysis (labeled CI 1

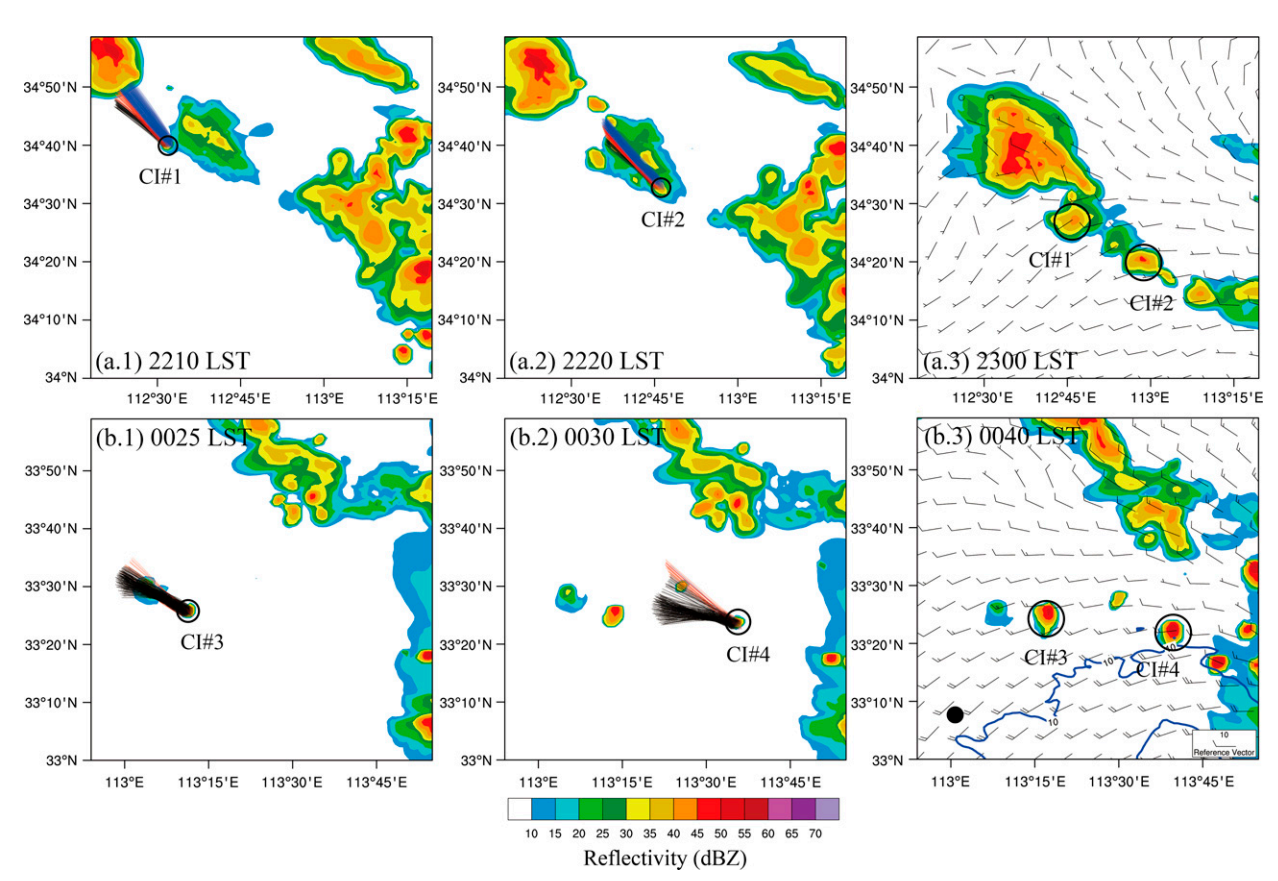


FIG. 7. Backward trajectories in the *x*–*y* plane within the strongest updrafts initialized when the reflectivity reached 35 dBZ and going backward in time for 30 mins. Each trajectory represents one parcel, and the color indicates the levels from which air parcels originate (black below 3000 m MSL, red at 3000–4000 m MSL, and blue above 4000 m MSL) with composite reflectivity (shading; dBZ) and [in (a.3) and (b.3)] 1500-m MSL winds. The open circles indicate the locations of the selected cells. The region with 1500-m MSL wind speeds over 10 m s⁻¹ is indicated by blue lines, representing the LLJ. The black dot indicates the location of the sounding in Fig. 13a, below.

and CI 2 in Fig. 7) as these cells played a role in evolving this arrow into a more linear feature. For arrow 2, the two cells were selected (labeled CI 3 and CI 4 in Fig. 7) to provide insight into the pristine CI that took place behind the bow echo and played a role in the formation of the 2nd arrow. Trajectory analysis for every cell began at the time when the maximum reflectivity of the selected cells reached 35 dBZ. Air parcels at three different altitudes of 4200, 4500, and 4800 m AGL are examined. At each altitude, a total of 100 parcels are sampled uniformly within a box, with a horizontal resolution of 300 m. The parcels were then traced backward for 30 min, using the fourth-order Runge–Kutta schemes described in Xu et al. (2017). Each of the trajectory analysis included 300 points traced backward in time.

As noted earlier, the local environment in the vicinity of the arrows contained strong vertical shear and the trajectory analysis provides insight into the origin of the air parcels feeding the convective cells within the arrows. The horizontal locations of the cells are shown in Fig. 7, while Fig. 8 depicts the vertical displacements along the trajectories at heights above mean sea level (MSL henceforth). In both Figs. 7 and 8, the heights of the trajectory origins are color coded (e.g., black

below 3 km MSL, red between 3 and 4 km MSL, and blue above 4 km MSL). From this analysis, the air within the cells forming the arrows generally originated to the NW and WNW of the cells (Fig. 7). The trajectories for the cells in arrow 1 originated over a wide variety of heights ranging between 2.2 and 4.8 km MSL in the first cell and 2.4–4.8 km MSL in the second (Figs. 8a,b) perhaps indicating a greater influence from the MCV. Recalling the results shown in Fig. 5, the wide range of the heights of the parcel origin suggests that the parcels in the lower levels are associated with southwesterly flow within the LLJ, while the parcels at higher levels are associated with the NW flow. Parcels originating from the MCV experiences gentler rising motion, while the LLJ oriented parcels experienced a greater upglide in altitude.

One difference between the cells within the two arrows is that the parcel trajectories in arrow 2 tended to originate at lower levels with the majority of the parcels originating between 1.8 and 3 km MSL in the first cell and between 1.5 and 2.5 m MSL in the second cell. The parcels originating at these levels were associated with the southwesterly flow associated with the LLJ. The parcels within arrow 2 also tended to have

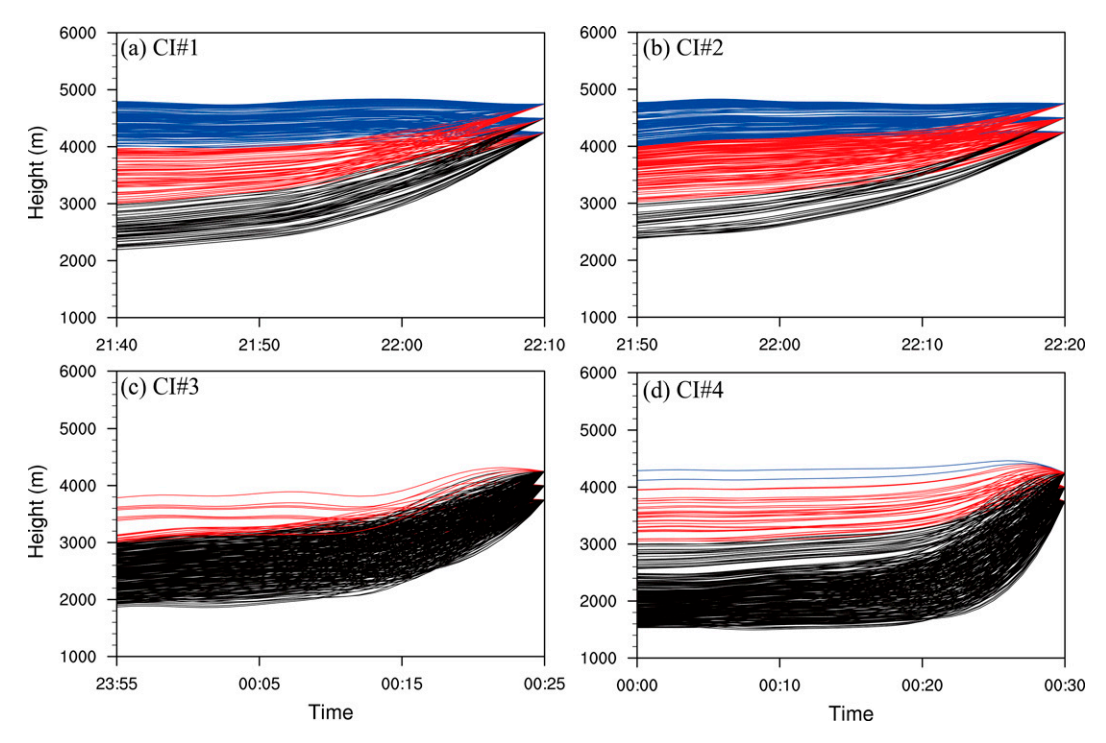


FIG. 8. Height at MSL along the backward trajectories of air parcels within the cells. The color of the trajectory indicates the levels from which air parcels originate, as noted in Fig. 7.

a much more pronounced ascent at later times (Figs. 8c,d) than the cells within the arrow 1 (Figs. 8a,b) consistent with the increase in the MUCAPE of the inflow air in the simulations (Figs. 6a,b). The ascent in the trajectories for arrow 2 is especially pronounced for the parcels originating at lower levels and for the second cell. Placing the trajectories within a framework of the MCS, all the air parcels were found to originate from altitudes above 1.5 km MSL, indicating that the convection is clearly elevated and not based in the NSBL. The rising updraft of the cells in arrow 1 from the low levels (i.e., originating from \sim 2.75 km MSL) are associated with the northwesterly flow of the MCV. In contrast for arrow 2, most air parcels were ingested into the cells from lower levels more closely associated with the LLJ's southwesterly flow, especially for the second cell where the trajectories have rapid ascent into the updraft core region during the final 15 min. The few trajectories originating aloft between 3 and 4 km MSL in arrow 2 would again likely be associated the MCV northwesterly flow, which is consistent with a closer inspection of the trajectories in the second cell within arrow 2 (Fig. 7).

This result is consistent with air parcels in the updrafts originating from the northwest and west-northwest of the cells (Fig. 7) rather than parcels being solely traced to the southwesterly flow associated with the LLJ. These findings from the trajectory analyses and the large vertical shear in the region where cells form suggest that dynamical processes, rather than parcel buoyancy alone may have played a role in the formation and organization of the cells within the arrows. This hypothesis will be investigated in the next section.

5. Dynamic forcing mechanisms and physical explanation

a. Dynamic forcing mechanisms

Vertical momentum budgets were applied in a Lagrangian framework and were calculated using Eqs. (4a)-(4e) substituted into the right-hand side of Eq. (3). The calculations were applied along backward trajectories for the parcels (in black originating below 3 km MSL) using output from the innermost domain at 1-min intervals. The average value of all the parcels in black were selected for investigation due to their significant ascent within the cells as shown earlier in Fig. 8. These average trajectories begin with relatively gentle ascent that is consistent with air gradually ascending over the cold pool before beginning a more rapid ascent. The vertical momentum budgets were used to investigate the causes for this more rapid ascent through examination of the dynamic/buoyant acceleration and the components of dynamic acceleration for the four selected cells shown in Figs. 9 and 10.

Common characteristic can be seen in cells 1, 3, and 4, with cell 2 having a more complex evolution. These common characteristics begin with small fluctuations in a_d and a_b as the parcels gradually ascend at lower levels prior to experiencing strong vertical acceleration. Another common characteristic is that a_d begins to substantially increase during the initial strong ascent with a maximum at a height of \sim 3500 m MSL within the layer of strong vertical shear (e.g., Fig. 6). The magnitude of a_d subsequently decreases abruptly and a_b increases with a similar trend but a smaller magnitude lagging several minutes in time behind the dynamic forcing term (Fig. 9). For

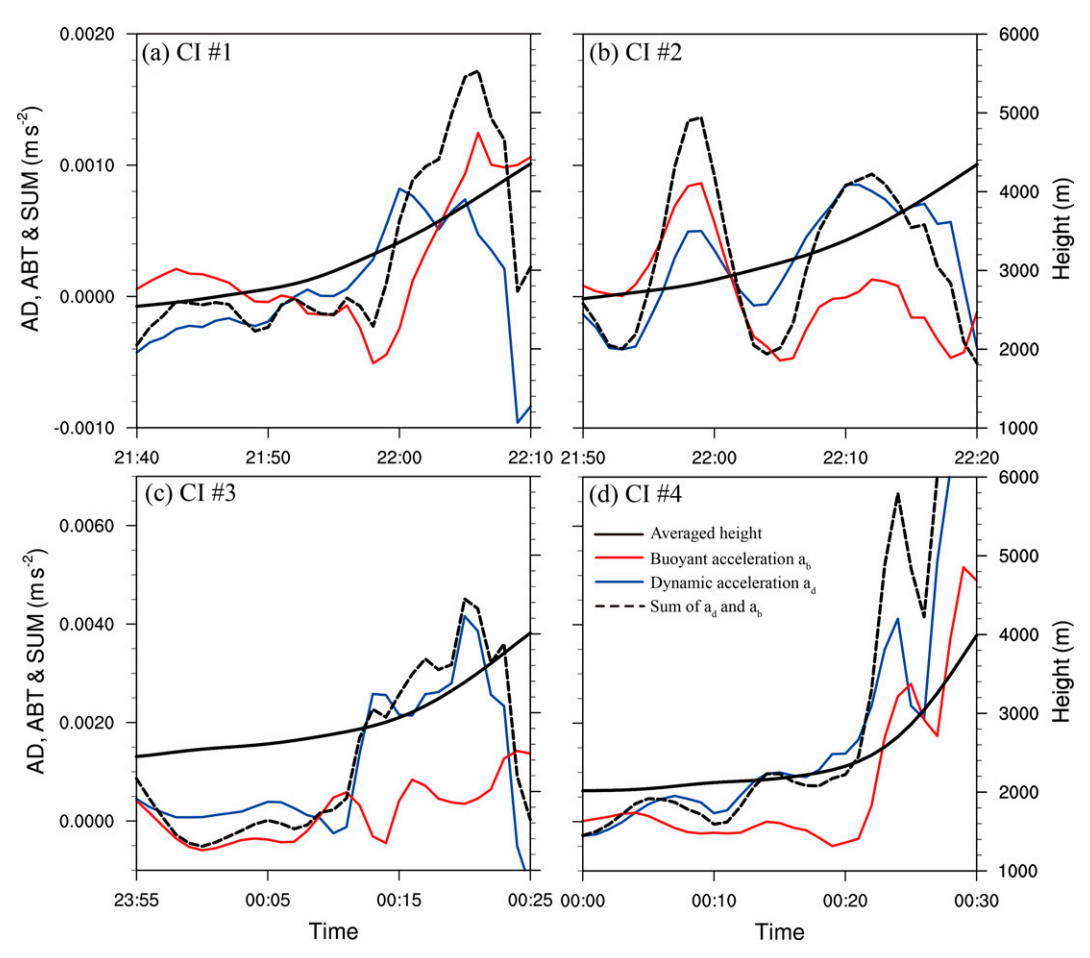


FIG. 9. Height (right y axis) above MSL and average vertical momentum budgets (left y axis) along the air parcels highlighted in black in Figs. 7 and 8. Note that the range of the left y axis for (a) and (b) differs from that for (c) and (d).

all arrow cells, the dynamic forcing dominates the strong early parcel ascent when the cells first form, although the buoyant forcing begins to play a more significant role at higher levels due to diabatic heating. Considering that a_b is generated by the convection itself (parcels should be freely accelerated upward above LCL), a_d probably does all of the work to get parcels to their LFC. For the complex evolution in cell 2, the first sudden peaks in magnitudes before 2200 LST may be a failed attempt of convection initiation (Figs. 9b and 10b). It is also worth noting that this analysis concentrated on the earliest stages of the convection to provide insight into the formation of the arrows. However, dynamic forcing played a similar role in initiating updrafts later when the cells matured, resulting in deeper convection (i.e., the air parcels arrived at heights of ~8 km MSL). Thus, dynamic forcing associated with vertical pressure perturbations due to the wind field, rather than buoyancy alone, are playing a critical role in the early formation and maintenance of convective within the arrows, with a maximum contribution in the layer where the flow is transitioning from vertical shear associated with the LLJ to that of the MCV.

Recognizing the importance of the dynamic forcing in the early initiation and maintenance of the convective updrafts, detailed analyses of the components of the dynamic forcing, a_d , were conducted to provide deeper insight into the factors governing the initial air parcels ascent within the convective cells (Fig. 10). The sum of the components of a_d exhibited similar trends as the results in Fig. 9, but with some small differences. From the decomposition of the terms contributing to a_d , it is apparent that the contribution to the acceleration from the vertical gradient of the vertical twisting term, that is,

$$2\overline{\rho}_{(z)}\left(\frac{\partial w}{\partial x}\frac{\partial u}{\partial z}+\frac{\partial w}{\partial y}\frac{\partial v}{\partial z}\right),\,$$

has the largest magnitude as the parcels begin their strong ascent at the LLJ/MCV interface. The vertical gradient of the horizontal curvature term, that is,

$$2\overline{\rho}_{(z)}\left(\frac{\partial v}{\partial x}\frac{\partial u}{\partial y}\right),$$

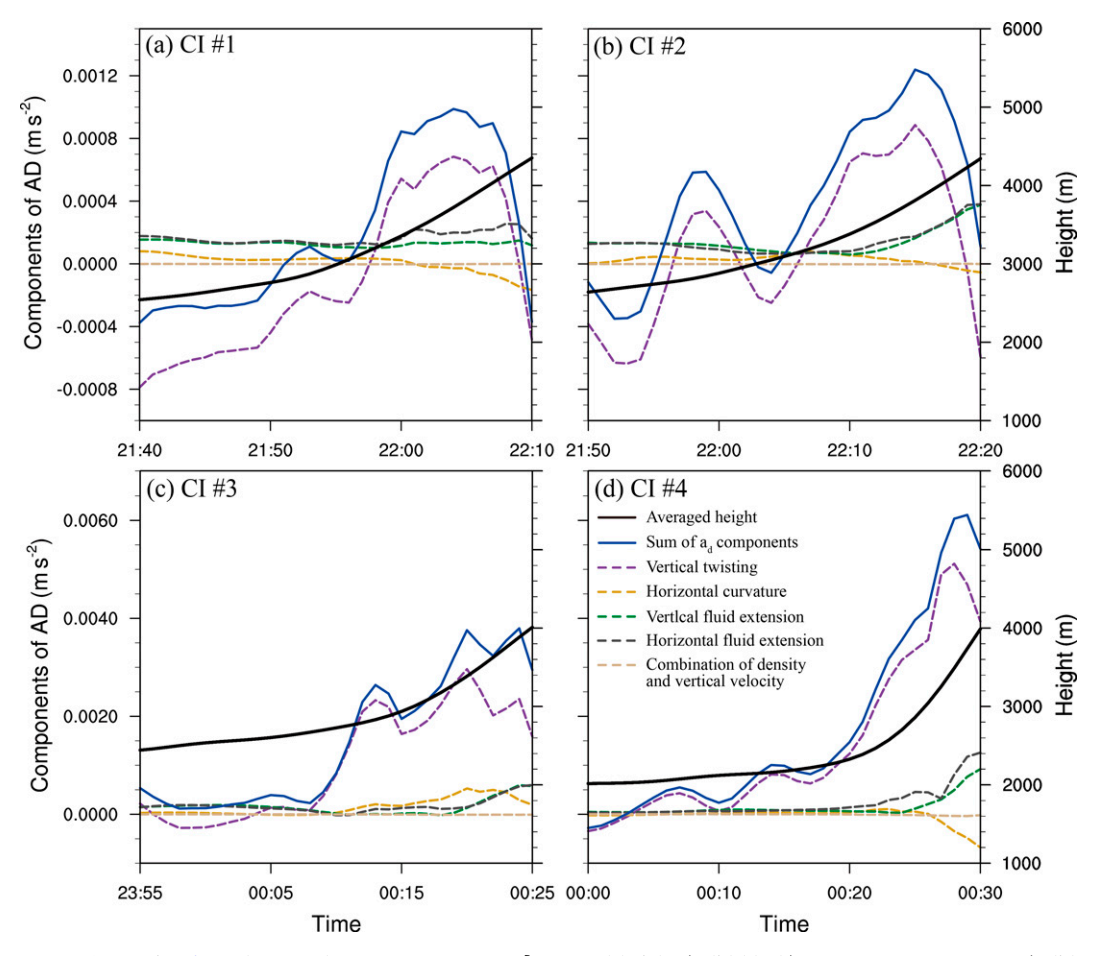


FIG. 10. As in Fig. 9, but for the components of a_d [averaged height (solid black), sum of a_d components (solid blue), vertical twisting (dashed purple), horizontal curvature (dashed yellow), vertical fluid extension (dashed green), horizontal fluid extension (dashed gray), and combination of density and vertical velocity (light brown)]. Note that the range of the left y axis for (a) and (b) differs from that for (c) and (d).

has a negative effect (negative acceleration) at higher levels. The vertical gradients in the two extension terms, that is,

$$\overline{\rho}_{(z)} \left[\left(\frac{\partial u}{\partial x} \right)^2 + \left(\frac{\partial v}{\partial y} \right)^2 \right] \quad \text{and} \quad \overline{\rho}_{(z)} \left[\left(\frac{\partial w}{\partial z} \right)^2 \right],$$

make relatively stronger contributions to ascent at lower altitudes 15 min prior to the onset of strong convection in arrow 1 (Figs. 10a,b) indicating the role of convergence between the LLJ and MCV, and possibly the gentle ascent over the cold pool on the initial ascent in these cells.

In interpreting these results, we note that the vertical twisting term is also sometimes referred to as the tilting of vertical shear by the updraft. The dominance of the vertical acceleration from the vertical gradient of the twisting term shows the importance of the interaction between the updraft and variations in the vertical shear. This interaction has been long known to be critical in supercell convection and helps explain why the supercells tend to occur in environments with large vertical shear (e.g., Rotunno and Klemp 1985). While supercells rely on the vertical shear within the ambient environment, the vertical shear in the region

behind the bow echo is created not only by the ambient environment, but through the changes in vertical shear associated with the MCV generated by the convection.

To summarize, the magnitude of a_d is much larger than a_b and thus dominates the updrafts during the early stages of convective ascent within the arrows. Just as the results of the trajectory analysis indicate, the parcels above the NSBL at low-mid levels are lifted in the region where a_d (vertical gradient of fluid extensions followed by that of vertical twisting) is concentrated, with a larger value of a_b at midlevels being a result of latent heating. The trajectory analysis implies that the gradual upglide of parcels within the LLJ over the cold pool likely assisted these lower in altitude parcels to reach their LFCs.

b. Physical explanation

To understand how vertical twisting dominates the dynamic forcing term, that is,

$$\frac{\partial w}{\partial x}\frac{\partial u}{\partial z} + \frac{\partial w}{\partial y}\frac{\partial v}{\partial z}$$

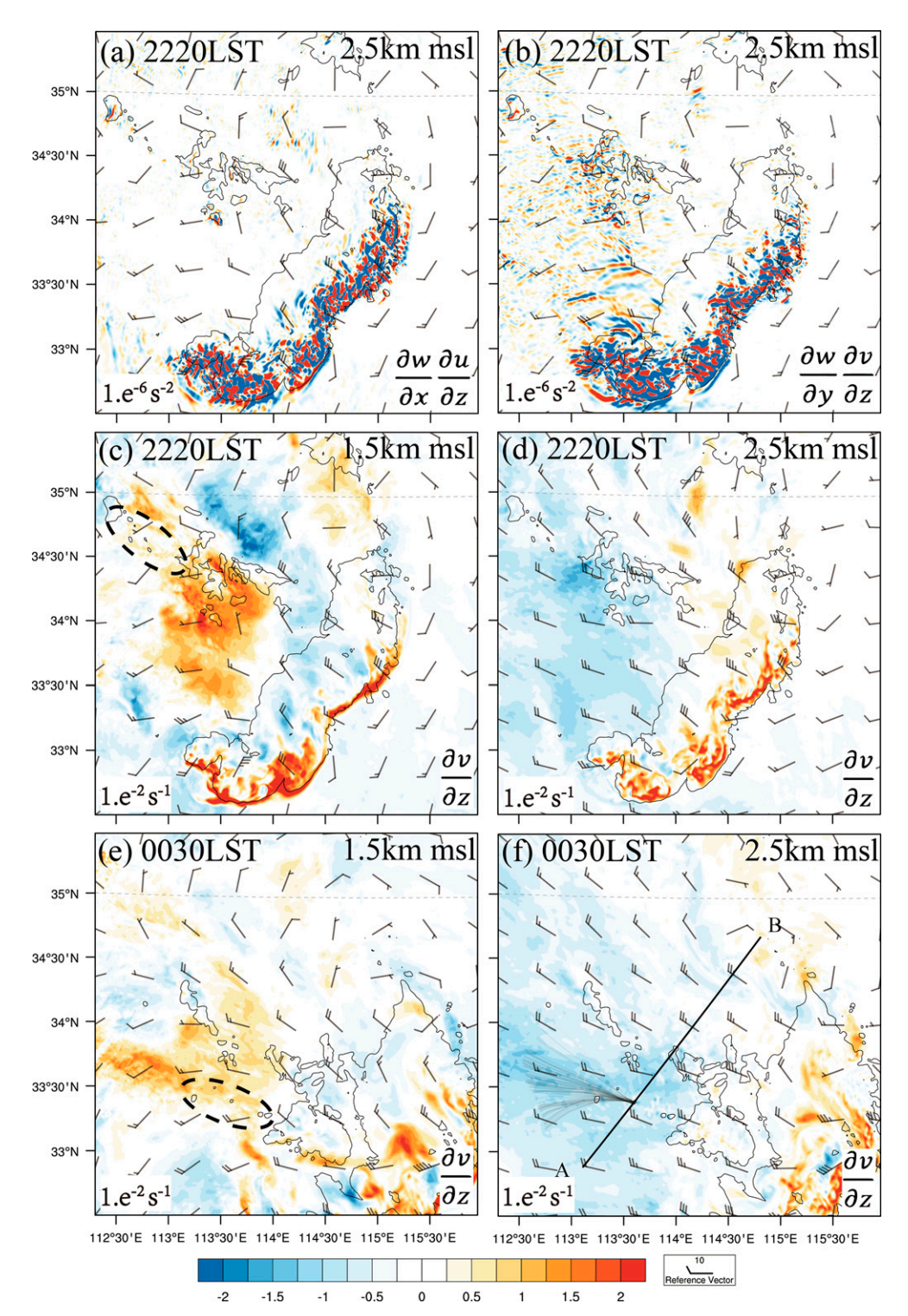


FIG. 11. Reflectivity of 35 dBZ (contours), wind barbs (kt) at 1.5 km MSL, and horizontal distribution of (a) $(\partial w/\partial x)(\partial u/\partial z)$ and (b) $(\partial w/\partial y)(\partial u/\partial z)$ (shading; $1 \times 10^{-6} \, \mathrm{s}^{-2}$) at 2.5 km MSL at 2220 LST. Also shown is the reflectivity of 35 dBZ (contours), wind barbs (kt), and horizontal distribution of $\partial u/\partial z$ (shading; $1 \times 10^{-2} \, \mathrm{s}^{-1}$) at (c),(e) 1.5 and (d),(f) 2.5 km MSL at (middle) 2220 and (bottom) 0030 LST. In (f), the black line labeled with A and B indicates the location of the cross section in Fig. 12, below, and the light-black trajectories are the backward trajectories of 150 min from cell 4. The dash-outlined ellipses in (c) and (e) respectively indicate the locations where cells selected in arrow 1 and 2 formed. All panels share the same color table.

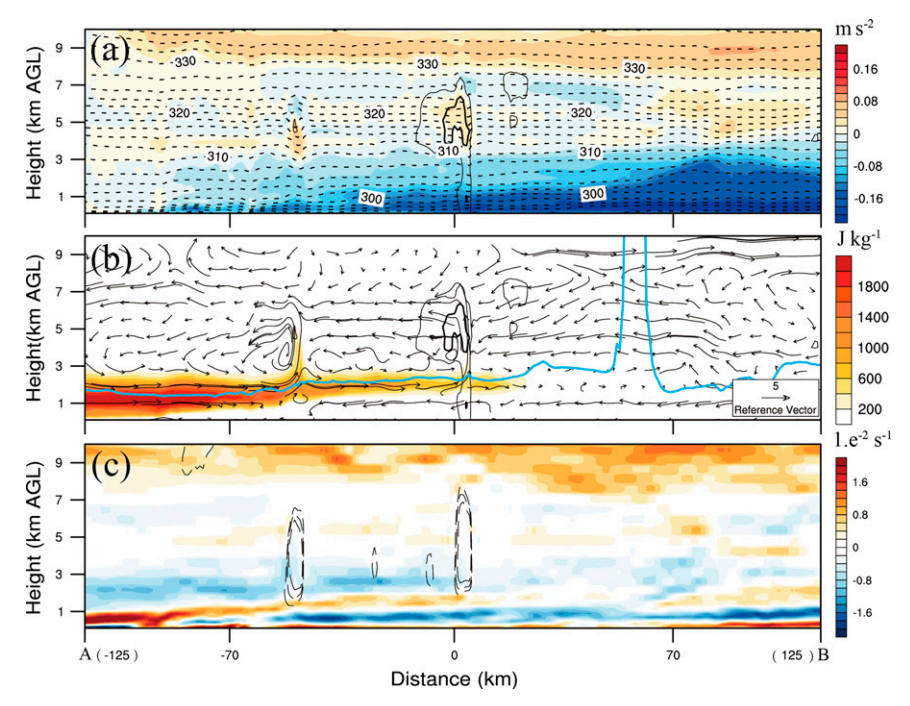


FIG. 12. Vertical cross section along AB in Fig. 11 at 0030 LST of (a) buoyancy (shading), 15- (thin contours) and 35-dBZ (thick contours) reflectivity, and potential temperature (dashed lines; K); (b) CAPE (shading), LFC (light-blue line), 15- (thin contours) and 35-dBZ (thick contours) reflectivity, and the ground-relative wind vectors along AB (m s⁻¹); and (c) $\partial u \partial z$ (shading) and vertical velocity (dashed contours at 0.5, 1.0, 2.0 m s⁻¹).

in our previous analysis, we decomposed the vertical twisting term into the separate terms $(\partial w/\partial x)(\partial u/\partial z)$ and $(\partial w/\partial y)(\partial v/\partial z)$. In the region where the cells within the arrow form, $(\partial w/\partial y)(\partial v/\partial z)$ is likely to be the dominant term, and we further explored this result by decomposing the term into $\partial w/\partial y$ and $\partial v/\partial z$. Our results show that $\partial w/\partial y$ is much smaller than $\partial v/\partial z$, with $\partial w/\partial y$ exhibiting a broader distribution of magnitudes at the upstream of the bow, particularly in the vicinity of the arrows (not given). The broader upstream distribution of ∂w ∂y is generated by a gradual upglide of parcels atop the cold pool, followed by additional convergence at the LLJ/MCV intersection. The distribution of $\partial w/\partial y$ could be regarded as homogeneous before the formation of the arrow. The $\partial v/\partial z$ distribution is not homogeneous, however, as shown at different levels for 2220 and 0030 LST in Figs. 11c-f, when strong convective ascent within the cells were initiated in each arrow. This analysis shows that there is a strong sign reversal as $\partial v/\partial z$ in the location where the arrows form with positive values in the lower levels and negative values in the middle levels. The positive $\partial u/\partial z$ is associated with the intrusion of the elevated SW flow associated with the LLJ, while the negative $\partial v/\partial z$ results from the influence of the NW flow associated with the MCV. At 2220 LST, the positive and negative terms are generated over a broader area with high vertical wind shear and the formation of the convective cells tended to occur in a cluster (Figs. 11c,d). At 0030 LST, the area of both the high vertical wind shear and

the convection becomes more linear leading to the formation of arrow 2.

From Figs. 11c-f, it is clear that the sign and magnitude of the vertical shear changes significantly with height in the vertical layer between 1.5 and 2.5 km MSL. Thus, as parcels in the convective arrows initially move upward from the layer containing the LLJ, the sign of the vertical twisting term will change. Recall that the dynamic contribution to the vertical acceleration in Eq. (1) is due to the vertical gradients of the dynamic terms in Eq. (4), with the change in sign influenced by the Laplacian. It follows that the reversal in sign of the vertical twisting term from positive to negative will enhance updraft intensity. Thus, the change in vertical shear from the LLJ to the MCV would create a low pressure perturbation p'_d , supporting a favorable layer for dynamic forcing that promotes ascent through a favorable vertical pressure gradient.

A clearer view of the structure and interaction between the LLJ and MCV is provided in Fig. 12 along the line AB in Fig. 11 when cell 4 was initiated within the second arrow. The buoyancy field in Fig. 12a was calculated following the approach utilized in Adams-Selin and Johnson (2013) and Blake et al. (2017):

$$B \equiv g \left[\frac{\theta'}{\overline{\theta}} + 0.61(q_v - \overline{q}_v) - q_c - q_r - q_i \right], \tag{5}$$

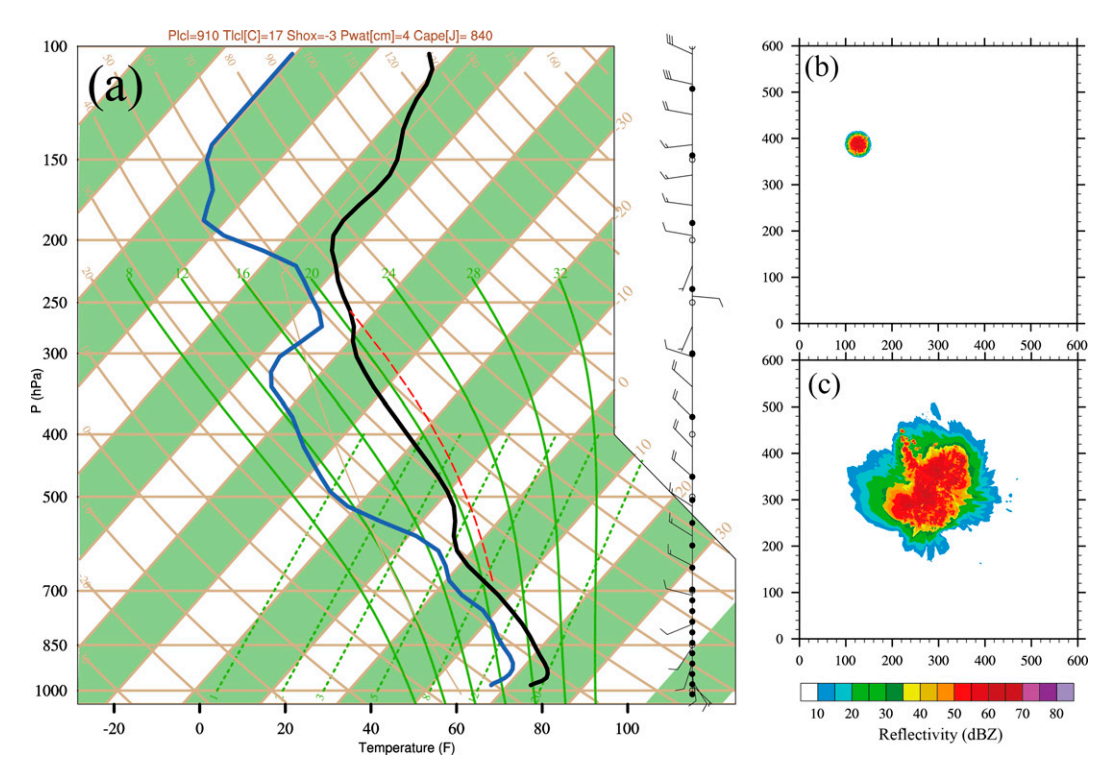


FIG. 13. (a) The thermodynamic sounding used in the idealized experiment plotted in a skew T-logp format. The sounding was obtained from the WRF-ARW domain 3 within the LLJ region as described in section 3. The vertical profile of the horizontal wind is shown on the right-hand side of the plot (wind barbs; m s⁻¹). Also shown is composite reflectivity of the ideal experiment at (b) 50 and (c) 300 min.

where θ' is the difference between θ and $\overline{\theta}$, q_v represents the water vapor mixing ratio of the air in the inflow LLJ, q_c is the cloud water mixing ratio, q_r is the rainwater mixing ratio, and q_i is the mixing ratio of frozen condensate. The terms in the buoyancy equation were calculated as a function of height relative to air in the inflow LLJ within the 1-km model domain. In this calculation, the reference air mass (with the attribution of base state variables $\overline{\theta}$ and \overline{q}_v) is a function of height and time averaged over a 5 km \times 5 km box in the horizontal directions.

The buoyancy field in this cross section indicates a deep cold pool underneath the MCV. The cold pool (high magnitudes of negative buoyancy in Fig. 12a) spreads southwest and encourages gentle isentropic lifting from southwest to northeast with two areas of strong ascent. A NSBL is in place near the cells with a height of ~800 m above ground level (Fig. 12a). A layer of elevated CAPE in the nearsurface layer is transported northward by the LLJ, assisting in lifting parcels to their LFC and fostering convection (Fig. 12b). This elevated CAPE is also ingested into the cells. In Fig. 12c, the distribution of $\partial v/\partial z$ indicates the presence of vertical directional and speed shear. The first layer of negative vertical shear existing just above the surface indicates the northerly winds extending south from the cold pool. The layer of positive values of vertical shear from southwest to northeast indicates an increase of the wind

speed associated with the LLJ, while the second negative layer is produced by the MCV flow aloft. Hence, the lift of the convective parcels shown in Fig. 12 are enhanced within a layer containing a negative–positive–negative vertical shear pattern induced by the overlaying of flows from the cold pool, LLJ, and MCV. Our trajectory analysis (Figs. 9 and 10) shows that the upward acceleration in this layer leads to dynamical lifting of parcels to their LFC, with the contribution of the vertical gradient of the vertical twisting term supporting new convection.

6. Idealized simulations

An idealized experiment was conducted to investigate the formation of the convective arrows utilizing ambient horizontal wind profiles. As mentioned in section 3b, a warm bubble was utilized to provide the initial updrafts (i.e., $\partial w/\partial y$). A WRF point-forecast sounding, sampling the vertical wind profile at the LLJ/MCV interface, was used to generate an ambient kinematic environment (with a strong sign reversal of $\partial u/\partial z$) that would be favorable for arrow convection (Fig. 13a). The results of the simulations show that the convective cells move roughly with the mean northwesterly flow at the lower levels as evidenced by comparing the early formation of convection (Fig. 13b) with the subsequent depiction of

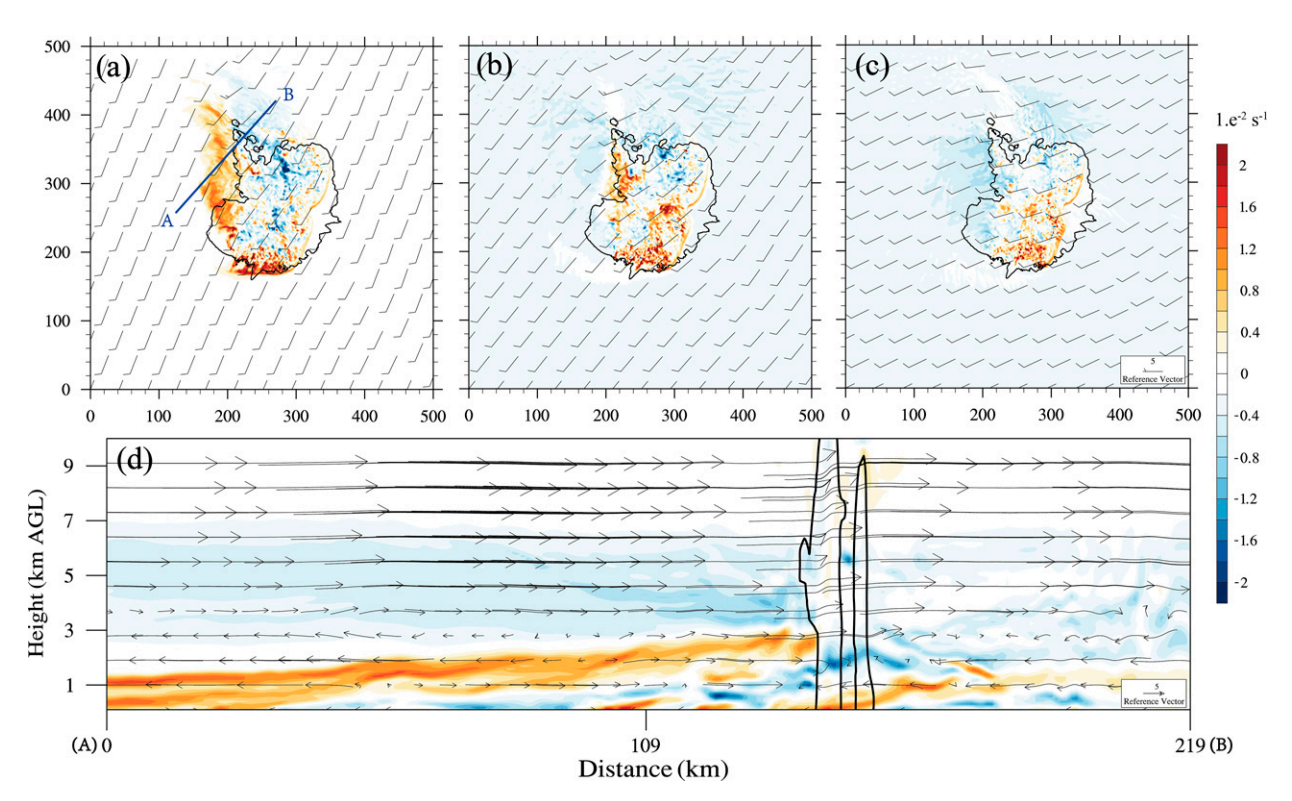


FIG. 14. Composite reflectivity of 35 dBZ (contours), wind barbs (kt), and horizontal distribution of $\partial u/\partial z$ (shading) at (a) 2, (b) 3, and (c) 4 km MSL at 300 min. The blue line labeled with A and B indicates the location of the cross section showing (d) 35-dBZ reflectivity (contours), the ground-relative wind vectors (m s⁻¹), and $\partial u/\partial z$ (shading). All panels share the same color table.

the MCS (Fig. 13c). An arrow is created behind the convection (Fig. 13c), likely due to the changing vertical shear (Fig. 14). Strong sign reversal of $\partial u/\partial z$ is again shown in the vicinity of the location where the arrow forms, with positive values in the lower levels and negative values in the middle levels (Figs. 14a–c). In Fig. 14d, similar to that in Fig. 12c, the existence of first layer of negative vertical shear just beneath the convection indicates northerly winds extending south associated with the convective downdraft. The layer of positive values indicates an increase of the wind associated with the background southwesterly LLJ. The origin of the second layer of negative $\partial u/\partial z$ is unclear, because no MCV develops in the simulation, but the wind perturbation associated with the convective arrow is a possible reason for this layer.

The previously utilized trajectory analysis and vertical momentum budgets were again applied to two cells in the CM1 run (the first cell of the arrow and the second cell initiated after the arrow formed; Fig. 15). The goal was to determine if dynamic forcing, driven by strong vertical shear at the LLJ/MCV intersection, supported the CM1-simulated arrow convection in the same manner as the WRF-based run. Results showed that the parcels began with gentle ascent at lower altitudes, followed by a more rapid ascent closer to the time of arrow convection initiation (Figs. 15c,d). The air

parcels at lower altitudes were associated with the SW flow in the idealized simulation. In this simulation there was again a maximum in a_d early in the parcel ascent (Figs. 16a,b) with a secondary role played by the fluid extension terms, followed by the vertical twisting term becoming the dominant term during the rapid rise of air parcels (Figs. 16c,d). These results support the notion that air within the LLJ experiences gentle ascent over the cold pool and then converges with the MCV, enhancing the dynamic lift of parcels to their LFC and supporting arrow convective initiation.

7. Summary and discussion

The accurate prediction of the back building MCS, especially the bow-and-arrow structure in the warm season remains a challenge for NWP models (Keene and Schumacher 2013; Lawson and Gallus 2016). Based on a successfully simulated bow-and-arrow MCS over China, our study supplements the previous systematic investigations of bow-and-arrow MCSs over North America (Keene and Schumacher 2013; Peters and Schumacher 2015, 2016; Hitchcock and Schumacher 2020). A unique aspect of this study is that we employed a detailed dynamic analysis to investigate the formation of convective cells within the arrow of a bow-and-arrow MCS. These detailed analyses included applying a parcel trajectory analysis and dynamical budgets to WRF-ARW simulations

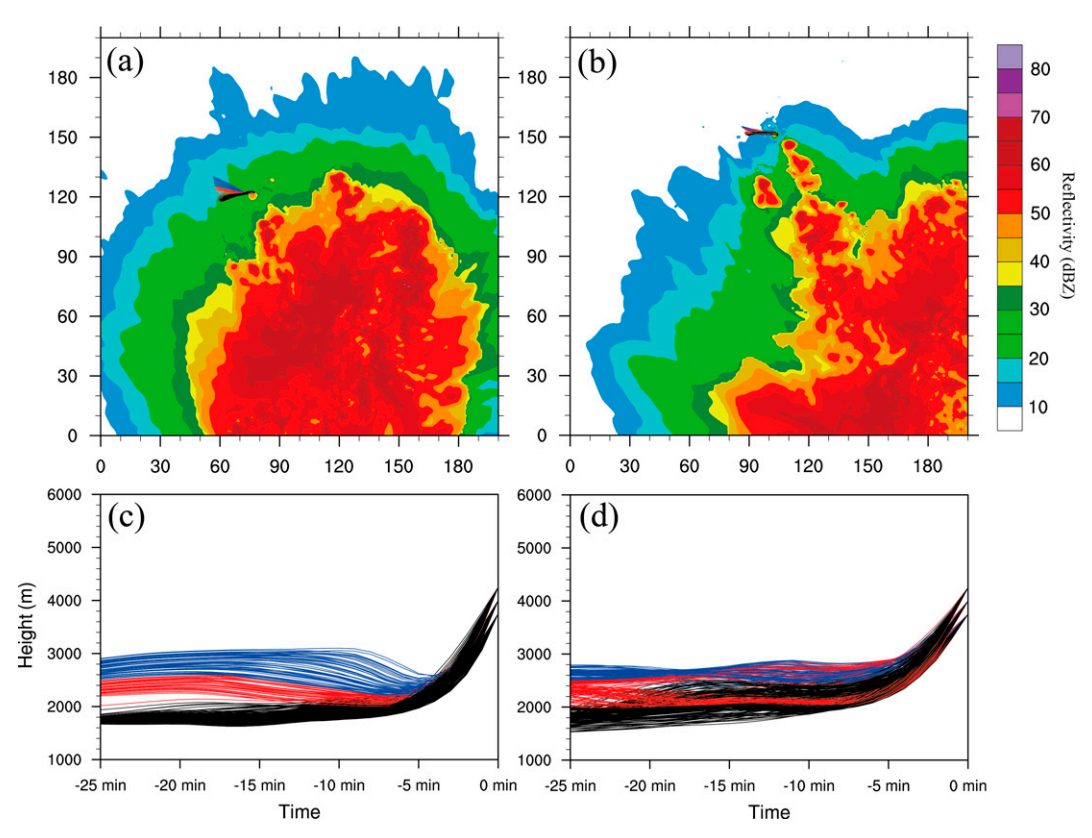


FIG. 15. Composite reflectivity of the CM1 experiment at (a) 202 min, early stage and (b) 270 min, development stage with backward trajectories in the *x*-*y* plane back to 30 min before. Each trajectory represents one parcel, and the color indicates the levels from which air parcels originate (black below 2000 m MSL, red at 2500–3000 m MSL, and blue above 3000 m MSL). (c),(d) The heights (above MSL) where the parcel trajectories in (a) and (b), respectively, were located out to 30 min in advance of arrow convection initiation. The color of the trajectory indicates the levels from which air parcels originate, as noted in (a) and (b).

via a Lagrangian framework. We also employed idealized CM1 simulations, as was undertaken in previous studies (Keene and Schumacher 2013; Peters and Schumacher 2016; Hitchcock and Schumacher 2020). However, we sought to go beyond these previous studies to quantify the relative role of the buoyant and dynamic forcing terms along the trajectories of air parcels that would support the initiation of arrow convection.

Our investigation revealed a synoptic situation similar to the findings of Keene and Schumacher (2013), with the convection in the arrow forming in an environment where high CAPE air in the LLJ gently rises over an extensive cold pool behind the leading edge of the MCS. Thus, the convective cells investigated herein are elevated as found in past studies (e.g., Keene and Schumacher 2013; Nielsen and Schumacher 2018). The dynamic analysis undertaken in our study shows that dynamic forcing dominates the initial formation of strong updrafts with these convective cells. The vertical superposition of the LLJ and convectively generated MCV created large values of vertical shear that enhanced the vertical acceleration of the parcels evident in the vertical twisting term. These results provide another example of how dynamic

forcing terms organize convection, such as in supercells and tornadoes (e.g., Rotunno and Klemp 1982; Davies-Jones 2003; Nielsen and Schumacher 2018). However, the vertical shear appears more complicated in bow-and-arrow MCSs as the shear is not just due to the environmental wind profile, but results from the interaction of the environmental LLJ ascending over the cold pool with the MCV generated by the MCS.

A conceptual model (Fig. 17) summarizes our results and depicts the LLJ transporting buoyant parcels from above the NSBL over a gently sloping cold pool behind the leading (bow) convective line. As this flow within the LLJ approaches the MCV, convergence is enhanced and updrafts are initiated. These air parcels are rising in a region where the vertical shear significantly changes across multiple layers from the cold pool, to the LLJ and the MCV. With the initial updrafts, the change of the large vertical shear with height enhances the dynamic forcing (a_d) through the change of the vertical twisting term with height in Eq. (4) that lifts the parcels to the LFC. Our conceptual model provides a 3D/2D representation to supplement Fig. 1 adapted from Keene and Schumacher (2013).

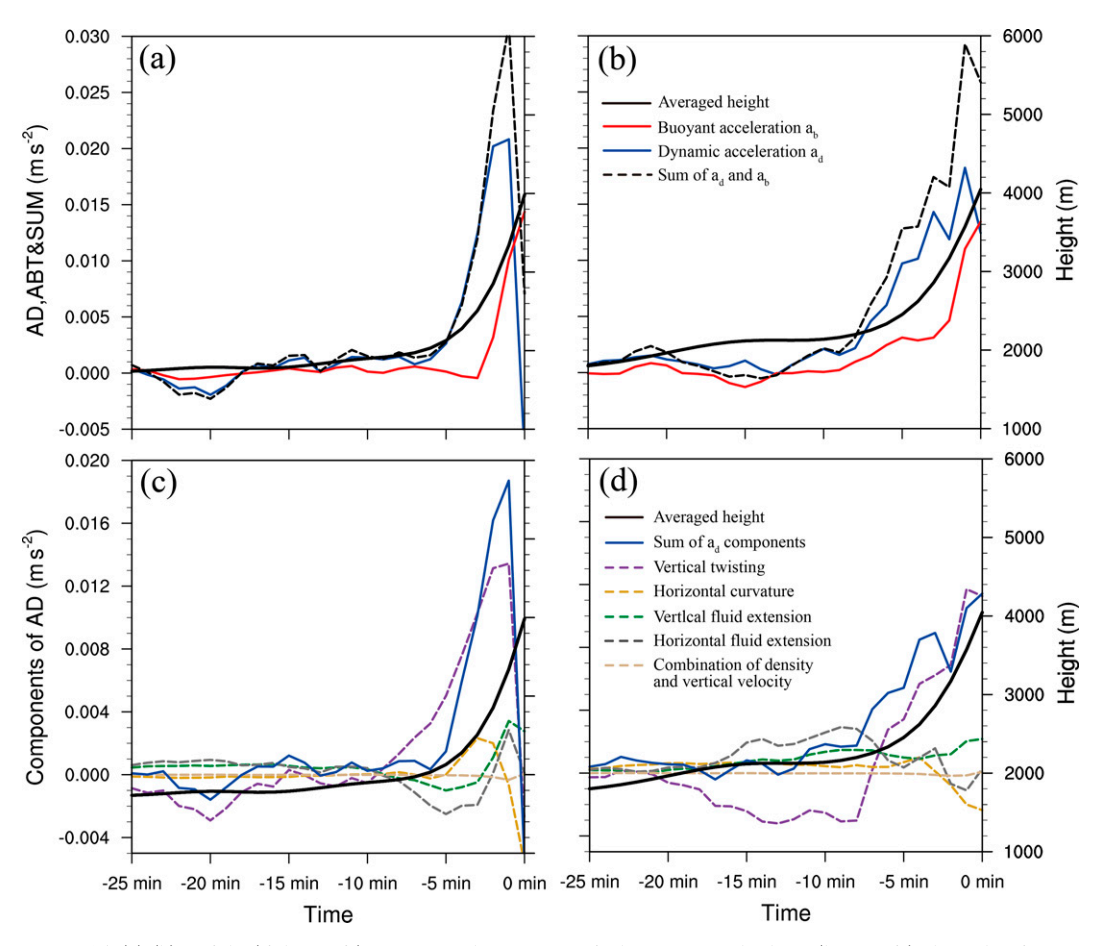
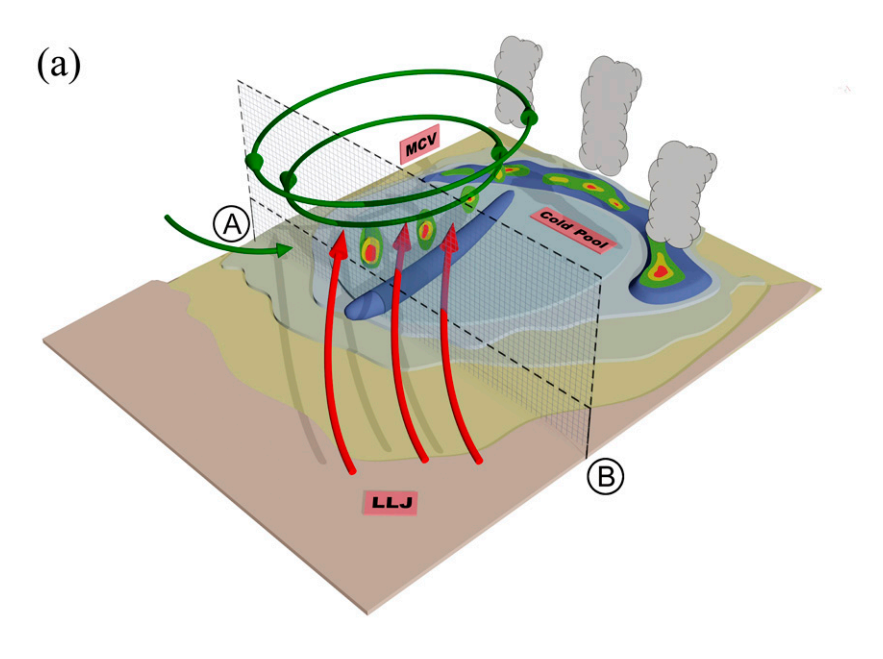


FIG. 16. (a),(b) Height (right y axis) at MSL and average vertical momentum budgets (left y axis) along the air parcels highlighted in black in Figs. 15c and 15d, respectively. (c),(d) As in (a) and (b), respectively, but for the components of a_d .

Other detailed findings and discussions are summarized below:

- 1) The general dynamic and thermodynamic characteristics of this MCS over China are similar to systems in the United States including: (i) the general structure with a bow-shaped echo at the leading edge of the MCS, lines of convection in the wake of the MCS defining the arrow and the presence of an MCV; (ii) the northwesterly flow associated with an MCV is juxtaposed with southwesterly flow associated with the LLJ; (iii) the LLJ transports warm and moist air behind the MCS leading line, restoring MUCAPE in the region of the arrow; (iv) gentle isentropic lifting of the LLJ air is provided by the spreading cold pool left by the bow; (v) the presence of baroclinicity to the south of the MCS.
- 2) To supplement Keene and Schumacher (2013), the two arrows investigated in this study confirm that the convergence between the LLJ and the MCV plays an important role in the initial parcel ascent and dominates the orientation of the arrow. However, our
- results show that the ascent within convective cells is subsequently enhanced by dynamic forcing within a deep layer of changing vertical shear created by the interaction between overlaying flows of the LLJ and MCV. This forcing appears critical in forming the convective cells within the two bands of convection within the arrow structure in the WRF and CM1 simulations. We acknowledge the possibility that either the $\partial v/\partial z$ or $\partial u/\partial z$ shear components of the twisting term may dominate depending on the orientations of the LLJ or bow-and-arrow MCS within a Cartesian framework. Still, the LLJ/MCV convergence behind the MCS leading line should still be the primary dynamic forcing mechanism to support arrow convective initiation.
- 3) The complex mesoscale processes contributing to bowand-arrow MCS development are challenging to simulate in convection-allowing models. Previous work has shown that sensitivities in the changes of ambient shear profiles alone can meaningfully impact MCS evolution. Further work could investigate how changes in vertical shear profiles or implementation of different physics configurations



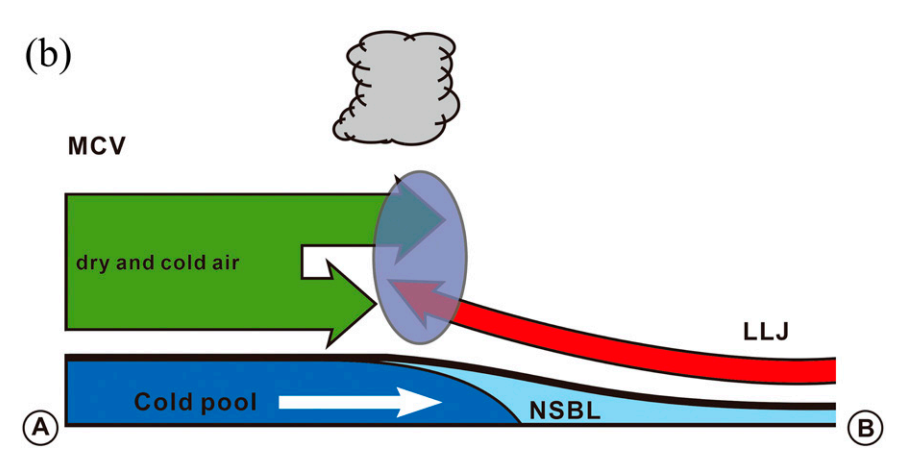


FIG. 17. Conceptual model of the LLJ and MCV interactions: (a) a 3D relationship and (b) a 2D relationship along the cross section indicated in (a). The blue ellipse indicates the region of the created deep-layer shear promoting ascent for subsequent convective initiation in the arrow region.

in convection allowing models impacts the development of arrow convection in MCSs.

Acknowledgments. This work was supported by National Natural Science Foundation of China 42122036, 42105007, 41875058, 42230607, and 91837207; The Open Grants of the State Key Laboratory of Severe Weather 2022LASW-B01; the Basic Research Fund of CAMS 2021Y016, 2021Z003; the General Program of Jiangsu provincial Meteorological Bureau KM202107; and the Jiangsu Innovative and Enterpreneurial Talent Programme JSSCBS20211317. The simulations were

conducted using the supercomputer at the School of Atmospheric Science, Nanjing University. The involvement of one of the investigators (David B. Parsons) is supported by NSF Grant AGS-1921587 with funding to enhance our understanding of bores and nocturnal MCSs. We appreciate discussions with Peter Bechtold (ECMWF) on the challenges of parameterizing nocturnal MCSs.

Data availability statement. The data used in this paper are large and only the core datasets were selected to upload. Supplementary data are accessible through contacting the author.

The observational data (including the radar and surface observations) that were used can be found online (https://doi.org/10.6084/m9.figshare.16944316.v1), as can the original and processed model data for Fig. 5 (https://doi.org/10.6084/m9.figshare.14716350.v1).

REFERENCES

- Abulikemu, A., Y. Wang, R. Gao, Y. Wang, and X. Xu, 2019: A numerical study of convection initiation associated with a gust front in Bohai Bay region, North China. J. Geophys. Res. Atmos., 124, 13 843–13 860, https://doi.org/10.1029/2019JD030883.
- —, and Coauthors, 2020: Mechanisms of convection initiation in the Southwestern Xinjiang, Northwest China: A case study. *Atmosphere*, 11, 1335, https://doi.org/10.3390/atmos11121335.
- Adams, J. C., 1989: MUDPACK: Multigrid portable FORTRAN software for the efficient solution of linear elliptic partial differential equations. *Appl. Math. Comput.*, 34, 113–146, https:// doi.org/10.1016/0096-3003(89)90010-6.
- Adams-Selin, R. D., and R. H. Johnson, 2013: Examination of gravity waves associated with the 13 March 2003 bow echo. *Mon. Wea. Rev.*, 141, 3735–3756, https://doi.org/10.1175/MWR-D-12-00343.1.
- Barnes, S. L., 1973: Mesoscale objective map analysis using weighted time-series observations. NOAA Tech. Memo. ERL NSSL-62, 70 pp., https://repository.library.noaa.gov/ view/noaa/17647.
- Bechtold, P., N. Semane, P. Lopez, J.-P. Chaboureau, A. Beljaars, and N. Bormann, 2014: Representing equilibrium and none-quilibrium convection in large-scale models. *J. Atmos. Sci.*, 71, 734–753, https://doi.org/10.1175/JAS-D-13-0163.1.
- Blake, B. T., D. B. Parsons, K. R. Haghi, and S. G. Castleberry, 2017: The structure, evolution, and dynamics of a nocturnal convective system simulated using the WRF-ARW Model. *Mon. Wea. Rev.*, 145, 3179–3201, https://doi.org/10.1175/ MWR-D-16-0360.1.
- Bryan, G. H., and J. M. Fritsch, 2002: A benchmark simulation for moist nonhydrostatic numerical models. *Mon. Wea. Rev.*, **130**, 2917–2928, https://doi.org/10.1175/1520-0493(2002)130 <2917:ABSFMN>2.0.CO;2.
- Chappell, C. F., 1986: Quasi-stationary convective events. Mesoscale Meteorology and Forecasting, P. S. Ray, Ed., Amer. Meteor. Soc., 289–310.
- Collins, W. D., and Coauthors, 2004: Description of the NCAR Community Atmosphere Model (CAM 3.0). NCAR Tech. Note NCAR/TN-464+STR, 214 pp., https://doi.org/10.5065/ D63N21CH.
- Corfidi, S. F., 2003: Cold pools and MCS propagation: Forecasting the motion of downwind-developing MCSs. *Wea. Forecasting*, **18**, 997–1017, https://doi.org/10.1175/1520-0434(2003)018 <0997:CPAMPF>2.0.CO:2.
- —, J. H. Meritt, and J. M. Fritsch, 1996: Predicting the movement of mesoscale convective complexes. *Wea. Forecasting*, 11, 41–46, https://doi.org/10.1175/1520-0434(1996)011<0041: PTMOMC>2.0.CO;2.
- Davies-Jones, R., 2003: An expression for effective buoyancy in surroundings with horizontal density gradients. *J. Atmos. Sci.*, **60**, 2922–2925, https://doi.org/10.1175/1520-0469(2003)060 <2922:AEFEBI>2.0.CO;2.
- Davis, C., and Coauthors, 2004: The Bow Echo and MCV Experiment: Observations and opportunities. *Bull. Amer. Meteor. Soc.*, 85, 1075–1094, https://doi.org/10.1175/BAMS-85-8-1075.

- Dawson, D. T., II, M. Xue, A. Shapiro, J. A. Milbrandt, and A. D. Schenkman, 2016: Sensitivity of real-data simulations of the 3 May 1999 Oklahoma City tornadic supercell and associated tornadoes to multimoment microphysics. Part II: Analysis of buoyancy and dynamic pressure forces in simulated tornado-like vortices. J. Atmos. Sci., 73, 1039–1061, https://doi.org/10.1175/JAS-D-15-0114.1.
- Haiden, T., M. Janousek, J.-R. Bidlot, R. Buizza, L. Ferranti, F. Prates, and F. Vitart, 2018: Evaluation of ECMWF forecasts, including the 2018 upgrade. ECMWF Tech. Memo. 831, 52 pp., https://doi.org/10.21957/ldw15ckqi.
- Hitchcock, S. M., and R. S. Schumacher, 2020: Analysis of back-building convection in simulations with a strong low-level stable layer. *Mon. Wea. Rev.*, 148, 3773–3797, https://doi.org/10.1175/MWR-D-19-0246.1.
- Houze, R. A., Jr., 2004: Mesoscale convective systems. Rev. Geophys., 42, RG4003, https://doi.org/10.1029/2004RG000150.
- Jeevanjee, N., and D. M. Romps, 2015: Effective buoyancy, inertial pressure, and the mechanical generation of boundary layer mass flux by cold pools. *J. Atmos. Sci.*, 72, 3199–3213, https://doi.org/10.1175/JAS-D-14-0349.1.
- Johns, R. H., 1993: Meteorological conditions associated with bow echo development in convective storms. Wea. Forecasting, 8, 294–299, https://doi.org/10.1175/1520-0434(1993)008<0294: MCAWBE>2.0.CO;2.
- Kain, J. S., 2004: The Kain–Fritsch convective parameterization: An update. J. Appl. Meteor. Climatol., 43, 170–181, https://doi.org/10.1175/1520-0450(2004)043<0170:TKCPAU>2.0.CO;2.
- Keene, K. M., and R. S. Schumacher, 2013: The bow and arrow mesoscale convective structure. *Mon. Wea. Rev.*, 141, 1648– 1672, https://doi.org/10.1175/MWR-D-12-00172.1.
- Klemp, J. B., and R. Rotunno, 1983: A study of the tornadic region within a supercell thunderstorm. J. Atmos. Sci., 40, 359–377, https://doi.org/10.1175/1520-0469(1983)040<0359:ASOTTR> 2.0.CO:2.
- Krueger, S. K., G. T. McLean, and Q. Fu, 1995: Numerical simulation of the stratus-to-cumulus transition in the subtropical marine boundary layer. Part II: Boundary-layer circulation. *J. Atmos. Sci.*, **52**, 2851–2868, https://doi.org/10.1175/1520-0469(1995)052<2851:NSOTST>2.0.CO;2.
- Lawson, J., and W. A. Gallus Jr., 2016: On contrasting ensemble simulations of two Great Plains bow echoes. Wea. Forecasting, 31, 787–810, https://doi.org/10.1175/WAF-D-15-0060.1.
- Liu, C., and M. W. Moncrieff, 2017: Shear-parallel mesoscale convective systems in a moist low-inhibition mei-yu front environment. *J. Atmos. Sci.*, 74, 4213–4228, https://doi.org/10.1175/JAS-D-17-0121.1.
- Lombardo, K., and T. Kading, 2018: The behavior of squall lines in horizontally heterogeneous coastal environments. *J. Atmos. Sci.*, 75, 1243–1269, https://doi.org/10.1175/JAS-D-17-0248.1.
- Mauri, E. L., and W. A. Gallus Jr., 2021: Differences between severe and nonsevere warm-season, nocturnal bow echo environments. Wea. Forecasting, 36, 53–74, https://doi.org/10.1175/WAF-D-20-0137.1.
- Miller, M. J., 1978: The Hampstead storm: A numerical simulation of a quasi-stationary cumulonimbus system. *Quart. J. Roy. Meteor. Soc.*, **104**, 413–427, https://doi.org/10.1002/qj. 49710444014.
- Morrison, H., and J. A. Milbrandt, 2015: Parameterization of cloud microphysics based on the prediction of bulk ice particle properties. Part I: Scheme description and idealized tests. *J. Atmos. Sci.*, 72, 287–311, https://doi.org/10.1175/JAS-D-14-0065.1.

- —, J. A. Curry, and V. I. Khvorostyanov, 2005: A new double-moment microphysics parameterization for application in cloud and climate models. Part I: Description. *J. Atmos. Sci.*, 62, 1665–1677, https://doi.org/10.1175/JAS3446.1.
- Nielsen, E. R., and R. S. Schumacher, 2018: Dynamical insights into extreme short-term precipitation associated with supercells and mesovortices. J. Atmos. Sci., 75, 2983–3009, https:// doi.org/10.1175/JAS-D-17-0385.1.
- Olson, D. A., N. W. Junker, and B. Korty, 1995: Evaluation of 33 years of quantitative precipitation forecasting at the NMC. *Wea. Forecasting*, **10**, 498–511, https://doi.org/10.1175/1520-0434(1995)010<0498:EOYOQP>2.0.CO;2.
- Parker, M. D., 2021: Self-organization and maintenance of simulated nocturnal convective systems from PECAN. Mon. Wea. Rev., 149, 999–1022, https://doi.org/10.1175/MWR-D-20-0263.1.
- Peters, J. M., 2016: The impact of effective buoyancy and dynamic pressure forcing on vertical velocities within two-dimensional updrafts. J. Atmos. Sci., 73, 4531–4551, https://doi.org/10.1175/ JAS-D-16-0016.1.
- —, and R. S. Schumacher, 2014: Objective categorization of heavy-rain-producing MCS synoptic types by rotated principal component analysis. *Mon. Wea. Rev.*, **142**, 1716–1737, https://doi.org/10.1175/MWR-D-13-00295.1.
- —, and —, 2015: The simulated structure and evolution of a quasi-idealized warm-season convective system with a training convective line. *J. Atmos. Sci.*, **72**, 1987–2010, https://doi. org/10.1175/JAS-D-14-0215.1.
- —, and —, 2016: Dynamics governing a simulated mesoscale convective system with a training convective line. *J. Atmos. Sci.*, 73, 2643–2664, https://doi.org/10.1175/JAS-D-15-0199.1.
- —, E. R. Nielsen, M. D. Parker, S. M. Hitchcock, and R. S. Schumacher, 2017: The impact of low-level moisture errors on model forecasts of an MCS observed during PECAN. *Mon. Wea. Rev.*, **145**, 3599–3624, https://doi.org/10.1175/MWR-D-16-0296.1.
- Pleim, J. E., 2006: A simple, efficient solution of flux-profile relationships in the atmospheric surface layer. J. Appl. Meteor. Climatol., 45, 341–347, https://doi.org/10.1175/JAM2339.1.
- —, 2007: A combined local and nonlocal closure model for the atmospheric boundary layer. Part I: Model description and testing. J. Appl. Meteor. Climatol., 46, 1383–1395, https://doi. org/10.1175/JAM2539.1.
- Przybylinski, R. W., 1995: The bow echo: Observations, numerical simulations, and severe weather detection methods. *Wea. Forecasting*, **10**, 203–218, https://doi.org/10.1175/1520-0434 (1995)010<0203:TBEONS>2.0.CO;2.
- Rotunno, R., and J. B. Klemp, 1982: The influence of the shear-induced pressure gradient on thunderstorm motion. *Mon. Wea. Rev.*, **110**, 136–151, https://doi.org/10.1175/1520-0493(1982)110 <0136:TIOTSI>2.0.CO;2.
- —, and —, 1985: On the rotation and propagation of simulated supercell thunderstorms. *J. Atmos. Sci.*, **42**, 271–292, https://doi.org/10.1175/1520-0469(1985)042<0271:OTRAPO>2. 0.CO;2.
- Schenkman, A. D., M. Xue, and D. T. Dawson II, 2016: The cause of internal outflow surges in a high-resolution simulation of the 8 May 2003 Oklahoma City tornadic supercell. *J. Atmos. Sci.*, 73, 353–370, https://doi.org/10.1175/JAS-D-15-0112.1.

- Schumacher, R. S., 2009: Mechanisms for quasi-stationary behavior in simulated heavy-rain-producing convective systems. J. Atmos. Sci., 66, 1543–1568, https://doi.org/10.1175/2008JAS2856.1.
- —, and R. H. Johnson, 2005: Organization and environmental properties of extreme-rain-producing mesoscale convective systems. *Mon. Wea. Rev.*, **133**, 961–976, https://doi.org/10. 1175/MWR2899.1.
- —, and —, 2009: Quasi-stationary, extreme-rain-producing convective systems associated with midlevel cyclonic circulations. Wea. Forecasting, 24, 555–574, https://doi.org/10.1175/ 2008WAF2222173.1.
- Skamarock, W. C., and Coauthors, 2008: A description of the Advanced Research WRF version 3. NCAR Tech. Note NCAR/TN-475+STR, 113 pp., https://doi.org/10.5065/D68S4MVH.
- Snively, D. V., and W. A. Gallus Jr., 2014: Prediction of convective morphology in near-cloud permitting WRF Model simulations. Wea. Forecasting, 29, 130–149, https://doi.org/10.1175/WAF-D-13-00047.1.
- Squitieri, B. J., and W. A. Gallus Jr., 2016: WRF forecasts of Great Plains nocturnal low-level jet-driven MCSs. Part II: Differences between strongly and weakly forced low-level jet environments. Wea. Forecasting, 31, 1491–1510, https://doi. org/10.1175/WAF-D-15-0150.1.
- Torri, G., Z. Kuang, and Y. Tian, 2015: Mechanisms for convection triggering by cold pools. *Geophys. Res. Lett.*, 42, 1943–1950, https://doi.org/10.1002/2015GL063227.
- Tseng, K.-C., E. A. Barnes, and E. D. Maloney, 2018: Prediction of the midlatitude response to strong Madden-Julian oscillation events on S2S time scales. *Geophys. Res. Lett.*, 45, 463– 470, https://doi.org/10.1002/2017GL075734.
- Vertz, N. J., W. A. Gallus Jr., and B. J. Squitieri, 2021: Can prestorm errors in the low-level inflow help predict spatial displacement errors in MCS initiation? *Atmosphere*, 12, 7, https://doi.org/10.3390/atmos12010007.
- Wei, P., and Coauthors, 2023: On the key dynamical processes supporting the 21.7 Zhengzhou record-breaking hourly rainfall in China. Adv. Atmos. Sci., 40, 337–349, https://doi.org/10. 1007/s00376-022-2061-y.
- Xu, K.-M., and D. A. Randall, 2001: Updraft and downdraft statistics of simulated tropical and midlatitude cumulus convection. *J. Atmos. Sci.*, 58, 1630–1649, https://doi.org/10.1175/1520-0469(2001)058<1630:UADSOS>2.0.CO;2.
- Xu, X., M. Xue, and Y. Wang, 2015: Mesovortices within the 8 May 2009 bow echo over the central United States: Analyses of the characteristics and evolution based on Doppler radar observations and a high-resolution model simulation. *Mon. Wea. Rev.*, 143, 2266–2290, https://doi.org/10.1175/MWR-D-14-00234.1.
- —, —, and H. Huang, 2017: Mechanisms of secondary convection within a Mei-Yu frontal mesoscale convective system in eastern China. J. Geophys. Res. Atmos., 122, 47–64, https://doi.org/10.1002/2016JD026017.
- Zhang, S., and Coauthors, 2020: A modeling study of an atmospheric bore associated with a nocturnal convective system over China. J. Geophys. Res. Atmos., 125, e2019JD032279, https://doi.org/10.1029/2019JD032279.
- ——, D. B. Parsons, X. Xu, J. Sun, T. Wu, F. Xu, W. Na, and G. Chen, 2022: Bores observed during the warm season of 2015–2019 over the southern North China plain. *Geophys. Res. Lett.*, 49, e2022GL099205, https://doi.org/10.1029/2022GL099205.